LRP 806/05 August 2005

Papers presented at the
Third IAEA Technical Meeting on
"ECRH Physics and Technology for ITER"
Como, Italy, 2 - 4 May 2005

IAEA Participants

(A color version of this LRP can be downloaded on: http://crppwww.epfl.ch/archives)

accepted for publication in
Journal of Physics: Conference Series

ISSN 0458-5895

Table of Content

Third-harmonic X-mode, real-time controlled top-launch ECW experiments on TCV Tokamak

S. Alberti[1], G. Arnoux[1], L. Porte[1], A. Bortolon[1], A. Karpushov[1], Y.Martin[1], S. Nowak[2], R. Pitts[1] and the TCV Team[1]

[1]Centre de Recherches en Physique des Plasmas (CRPP-PPB)
Association EURATOM - Confédération Suisse
Ecole Polytechnique Fédérale de Lausanne, CH-1015 Lausanne, Switzerland
[2]Istituto di Fisica del Plasma,
EURATOM-ENEA-CNR Association, Milano, Italy

E-mail: stefano.alberti@epfl.ch

Abstract. In the moderate magnetic field of TCV (1.5T), the recently installed X3 system (3 gyrotrons @118GHz, 0.45MW/each, 2s) broadens the operational space with the possibility of heating plasmas at high density, well above the cutoff density of the X2 system (X2 cutoff at $n_e = 4.2 \times 10^{19}\mathrm{m}^{-3}$). To compensate the significantly weaker absorption coefficient compared to the absorption of X2, the top-launch injection allows to maximize the ray path along the resonance layer thus maximizing the optical depth. To maintain the maximum absorption in plasma discharges with a dynamic variation of both density (refraction) and temperature (relativistic shift) a real time control system on the poloidal injection angle has been developped and succesfully tested on TCV. With a total injected power of 1.35MW and using the mirror real-time control, full-single pass absorption has been measured in an L-mode plasma. A significant fraction of the absorbed power is associated to the presence of suprathermal electrons generated by the X3 wave itself. In X3 heating experiments of H-mode plasmas it has been possible to enter into a different ELMy regime compared to the ohmic/low-power-heating ELMy regime. In these experiments a significant increase of the plasma energy is obtained with nearly full-single pass absorption. Results on the comparison of the absorbed fraction calculated with the TORAY-GA ray-tracing code and the beam-tracing code, ECWGB, which includes diffraction effects, are discussed.

1. Introduction

The use of electron cyclotron (EC) waves in magnetically confined plasmas such as tokamaks or stellerators has demonstrated in the past years the applications of EC waves in fusion relevant plasmas in terms of highly efficient localized heating and current drive [1], MHD control [2, 3, 4, 5] and formation and control of improved core electron confinement [6]. However, in overdense plasmas ($\omega_{pe}^2/\Omega_{ce}^2 >> 1$, ω_{pe} and Ω_{ce} being the electron plasma frequency and electron cyclotron frequency, respectively) EC heating (ECH) is restricted for wave frequencies ω near the fundamental cyclotron frequency and second harmonic because the wave is reflected by a cutoff layer before it can reach the resonance. One option for overcoming the density limit is the mode conversion from the O-mode or X-mode to the electron Bernstein wave (EBW) [7] which is also considered in TCV. The alternative which is presented in this paper is the 3^{rd} harmonic

in X-mode, which provides access to the density range frequently found in TCV (above the 2^{nd} harmonic X-mode cutoff), especially in H-mode discharges.

For a Maxwellian distribution function and a harmonic number $n \geq 2$, the optical thickness τ_{Xn} of the X-mode, launched from the low-field side (LFS) is proportional to the small term $(k_B T_e/m_e c^2)^{n-1}$ (in case of O-mode with quasi perpendicular injection the optical thickness τ_{On} is proportional to $(k_B T_e/m_e c^2)^n$ for $n \geq 1$); consequently the absorption of the X-mode at the third harmonic is significantly weaker than at the second harmonic. Contrary to the case of LFS injection, for a top launch configuration with a grazing incidence of the rf beam on the resonant layer, the optical depth τ_{X3top} scales as $\tau_{X3top} \sim T_e L$ with L being a characteristic length along the resonance layer [8].

In the moderate magnetic field of TCV (1.5T), the X3 system broadens the operational space with the possibility of heating plasmas at high density, well above the cutoff density of the X2, where the cutoff for the X2 and X3 waves are $4.2 \times 10^{19}\mathrm{m}^{-3}$ and $11.5 \times 10^{19}\mathrm{m}^{-3}$, respectively. The top-launch injection of the X3 wave maximizes the ray path along the resonance layer thus maximizing the optical depth, but it has the disatvantage of weak localization and poor control of the heating profile [8]. With a top launch configuration, the aiming accuracy is very critical because the characteristic width of the rf beam, w_0, is comparable with the characteristic width of the resonance layer, w_{res}. Hence, for maximizing the overlap of the rf beam on the resonance layer, a high accuracy of the launcher mirror angle is necessary. This aspect has motivated the implementation of a real-time feedback control on the mirror angle which will be described below. As explained in [8], the width of the resonance layer, w_{res}, is an increasing function of the electron temperature, and, in presence of a suprathermal electron population (SEP), an equivalent resonance layer width can be defined (w^*_{res} in [8]) which satisfies the following inequality $w^*_{res} > w_{res}$.

In this paper, the experimental configuration is presented in section 2. The real time control system of the mirror angle is presented in section 3. The X3 absorption studies performed with the real-time control of the mirror on L-mode plasmas are presented in section 4. In section 5, with 1.35MW of X3-ECH injected into an ELMy H-mode, results on a new ELMy regime (compared to the ohmic/low-power-heating of ELMy H-modes) are presented. A comparison of the experimental results with two different models: ray-tracing and beam-tracing are presented in section 6.

2. Experimental configuration

The recently completed ECH system on the TCV Tokamak, has a total of 4.5MW of installed power (4.05MW of injected power). It consists of 9 gyrotrons grouped in three "clusters" of three gyrotrons each [9]. Two of the clusters operate at 82.7GHz (0.5MW/gyrotron, 2s) and are used for heating and/or current drive, coupling to the X-mode EC plasma wave from the low-field side and being absorbed at the 2nd harmonic resonance (X2). The third cluster operates at 118GHz (0.5MW/gyrotron, 2s), couples to X-mode from the top of the vacuum vessel and provides the ECH power which is absorbed at the 3rd harmonic resonance (X3) [10].

As shown in Fig. 1, on the left, the three X3 waveguides radiate the rf beams onto a single toroidal mirror with a maximum incident power of 1.35MW. For the maximum rf pulse length in TCV of 2s, no cooling of the mirror is needed. The mirror is made of OFHC (Oxygen Free High Conductivity) copper ($246 \times 182.6 \times 10\mathrm{mm}^3$, 4kg) and has a 700mm focal length, focusing the beam inside the plasma. Assuming a gaussian distribution, its waist is $w_0 = 3.3$cm in E-field and is located approximately at the vacuum vessel center. The mirror can be steered radially from 800mm to 960mm from pulse to pulse and the mirror angle θ_l can vary from 40° to 50° during the shot with a maximum speed of $d\theta_l/dt = 20$ deg/s.

Drawings and pictures of different parts of the top-launch housing and its motorization are shown in Fig.2a-d. The friction-less flexure-pivots shown in Fig.2c are a key element for the real-

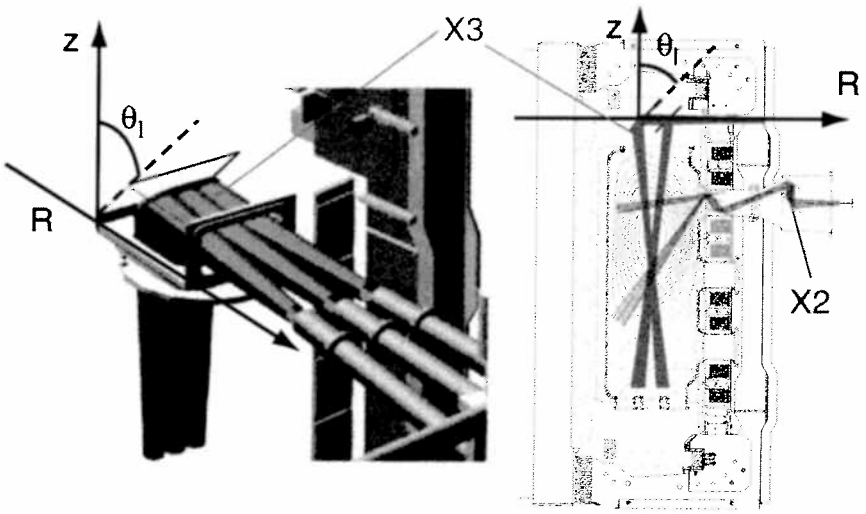

Figure 1. On left side, view of the X3 top-launch mirror. The three rf beams radiated from the HE_{11} waveguides are directed on one single focusing mirror which has radial and poloidal steering capabilities. The mirror angle, θ_l, can be controlled in real time. On the right side, a poloidal cross section of TCV, with shown, in red, the rf beam paths corresponding to the maximum radial steering range of the X3 launcher. In blue, the poloidal steering range of the X2 launcher.

time control of the mirror angle. Fatigue tests of this entire system over two years of operation has demonstrated very high reliability of this design. Similar flexure pivots are presently part of the design of the ITER front-steering launcher [11]. Fig.2 d, shows the transfer function represented in a Bode diagram (amplitude and phase versus frequency) of the mirror system and its motorization. A strongly damped resonance is observed around the frequency of 13Hz which is chosen as the driving frequency for the harmonic perturbation. The red curves represents an analytical fit with a second order pole ($G_2(s)$ in Fig.4). In general for real time control of such mirror systems, and in particular for the different EC launchers in ITER (upper port and equatorial) such a transfer function needs to be determined for each mirror to allow a proper design of the real-time feedback.

A key characteristic of the X3 top-launch heating is its sensitivity of the absorption to mirror angle as shown in Fig. 3 [8, 12]. For a given plasma equilibrium shown in Fig. 3b and a fixed mirror radial position the plasma response versus mirror angle is shown in Fig. 3a. With 0.45 MW of injected power, the level of absorption is indicated on this figure by the variation of the central temperature (T_{eX}, blue curve) deduced from the soft X-ray emission measurement along a central vertical view line by using the two-foil method (the method is based on the ratio of X-ray emissivities passing through two different low-pass filters [13]). As a comparison, the calculated absorption with the TORAY-GA code is shown in red. The optimum injection angle and the width of the absorption curve are in good agreement between the experiment and the simulation. The calculated X3 top-launch absorption versus mirror angle and radial position of the launcher is shown in Fig. 3c. The target plasma cross section is shown in the inserts and the absorption has been calculated on an experimentally obtained plasma equilibrium having a central electron density and temperature of $4. \times 10^{19}\mathrm{m}^{-3}$ and $2.7keV$, respectively. One notices that the FWHM of the absorption versus mirror angle is weakly dependent on the radial position.

The absorption sensitivity on the mirror angle θ_l has been experimentally studied in previous experiments and is also modelled by numerical simulations with TORAY-GA. For

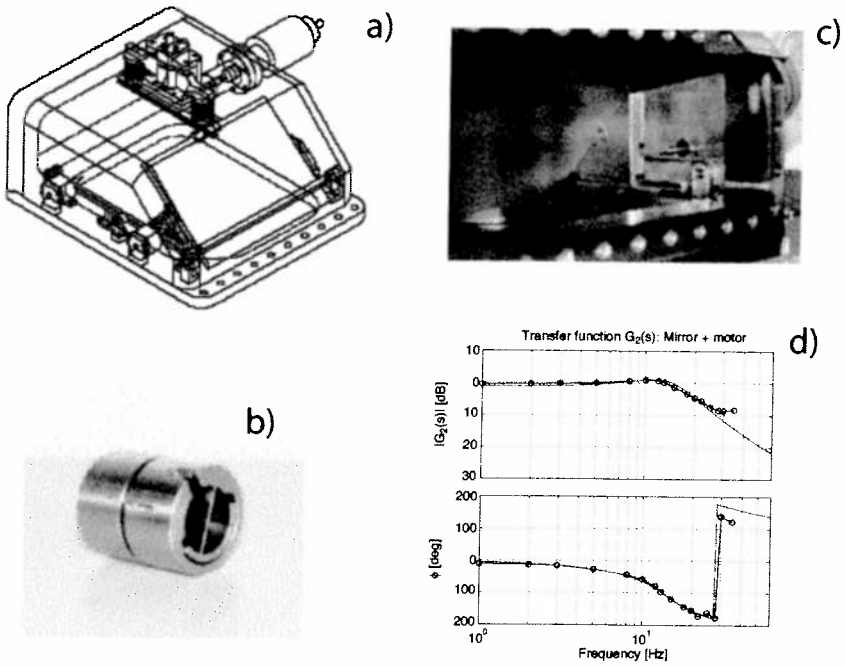

Figure 2. a) Schematic of the top-launch mirror. b) Picture of the frictionless bearings (Flexure-pivots) used for the mirror angle movement. c) Picture of the mirror with shown the chain system allowing the radial movement between shots. d) Frequency response of the mirror+motorization system represented in a Bode diagram (amplitude and phase).

a given plasma with fixed temperature and density profiles, the numerical simulation shows that the optimum mirror angle (at a fixed mirror radial position) depends on the central temperature and density with a sensitivity of $d\theta_l/dT_{e0}|_{n_e} = 0.2$ deg/keV (relativistic shift) and $d\theta_l/dn_{e0}|_{T_e} = 0.18$ deg/$(n_e\, 10^{19}\, \mathrm{m}^{-3})$ (refraction). This high sensitivity has motivated the development of a real time control of the mirror angle.

3. Real time control of the mirror angle

The real-time control is based on a sinusoidal modulation of the mirror angle and a synchronous demodulation of the plasma response. With this system it is possible to generate an error signal which is proportional to the derivative $dI_x/d\theta_l$ (or $dT_{eX}/d\theta_l$ in Fig. 3a) where I_x is the soft-X ray emissivity measured along a vertical chord passing through the plasma axis. A schematic of the analogue feedback system is shown in 4. The harmonic perturbation at 13Hz is used both for applying the sinusoidal perturbation on the launcher mirror and also as an input of the synchronous demodulator which is placed after a pass-band filter centered at 13 ± 5Hz. At the output of the demodulator the AC component is filtered out by a low-pass filter ($f_{cutoff} = 2$Hz) with the resulting signal being proportional to the derivative of the plasma response function, $dI_X/d\theta_l$. The dynamic response of the closed-loop system can be adjusted by the parameters of the PID (Proportional, Integral, Derivative) controller.

The dynamic response of the open-loop system is shown in Fig.5, where the different traces, labeled from a) to d), correspond to the points a) to d) indicated on Fig.4. Trace d) is the error signal which is proportional to the slope $dI_x/d\theta_l$. On trace c) one notices that the envelope of the signal at the pass-band filter output crosses zero exactly at the time ($t_1 = 1.41$s) when the mirror is at the optimum angle. The small time delay between this time, t_1, and the time of

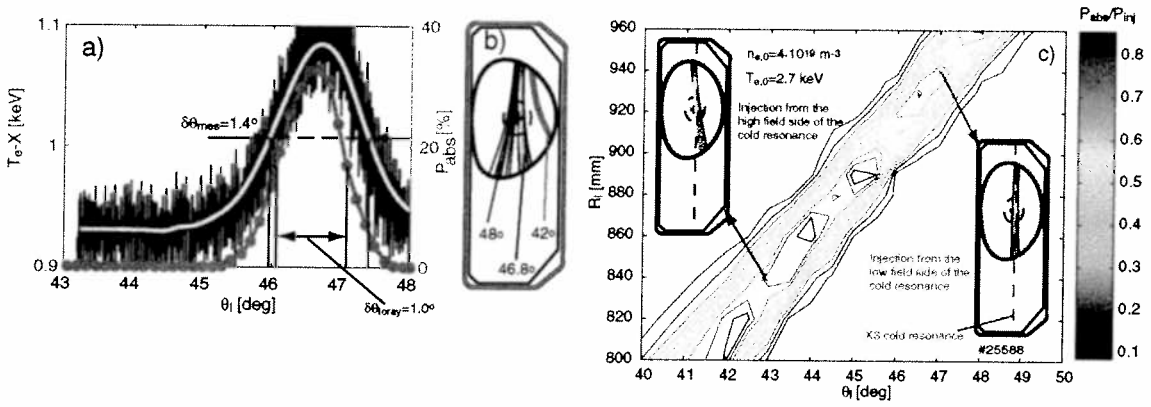

Figure 3. a) Blue trace: plasma temperature, T_{eX}, versus mirror angle (the yellow trace is the result of low-pass filtering the blue trace). In red, the absorbed fraction as predicted by TORAY-GA. b) Cross section of the plasma with ray trajectories for different injection angles. c) Contour plot of calculated absorbed fraction (ray-tracing code TORAY-GA) versus mirror angle and radial position of the mirror.

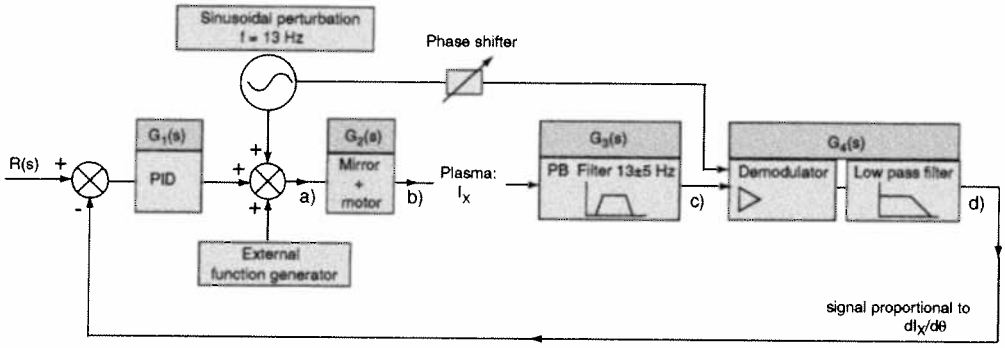

Figure 4. Schematic of the complete closed-loop feedback system.

zero crossing of trace d) ($t_2 = 1.47$s) is caused by the low-pass filter. This small difference can be compensated by adjusting the level of the reference signal $R(s)$.

In the closed loop system, this error signal is compared to an externally preset reference ($R(s)$ in Fig.4). The difference between the error signal and the reference is fed to a PID controller. For both, a P-term and a PI-term in the PID controller, studies of the dynamic response of the closed-loop system have been carried out on a wide variety of plasmas and mirror radial launching positions. The I-term has the property to bring to zero the steady state error as it is shown on Fig.6 (left figure third trace from top). It has also been verified that the system is able to track the optimum angle when an external preprogrammed ramp forces the mirror angle to move away from its optimum value[12]. It is planned to transform this analogue feedback system to a digital one.

The dynamic response of the closed-loop system with a PI controller is shown in Fig.6 where the external preset mirror angle was fixed at a value of 45.5deg. After a transient period of approximately $\tau_t = 250$ms, the mirror angle has reached a stationary optimum value. For fixed parameters of the PI-controller, the experimentally measured characteristic time for the transient period is linearly increasing with the plasma density[12].

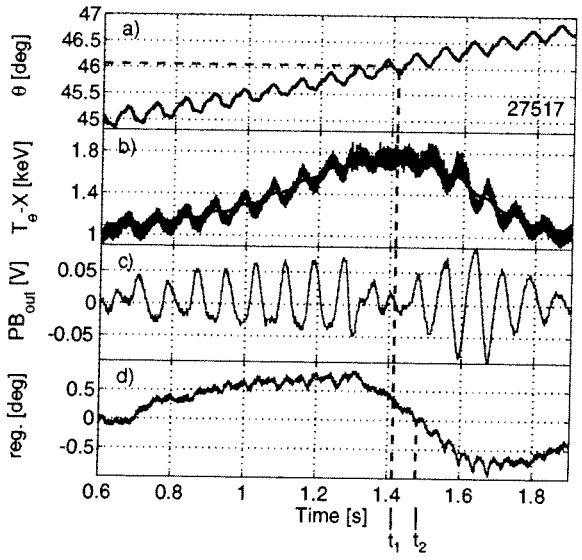

Figure 5. Open-loop signals during a linear sweep of the mirror angle where a linear angular sweep is performed such to cross the optimum mirror angle. On this linear sweep there is superimposed the sinusoidal modulation at 13Hz. The different traces labeled a) to d) correspond to the points a) to d) indicated on Fig.4

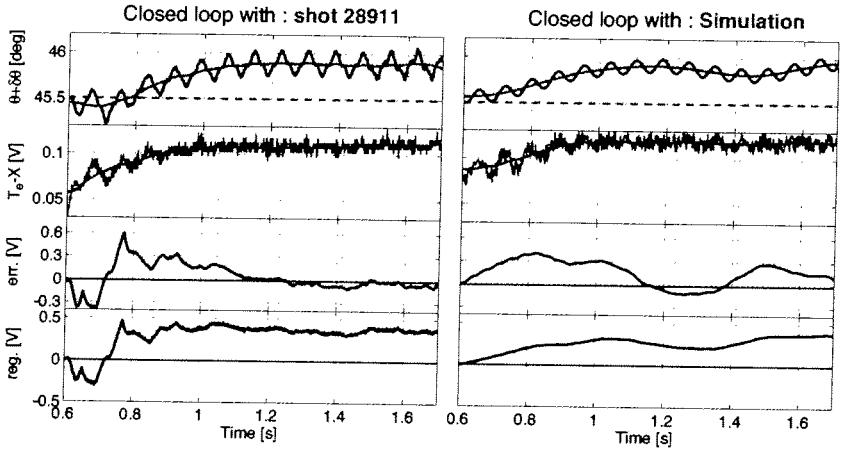

Figure 6. On the left, dynamics of the closed-loop feedback system on a plasma shot where the external reference has been set to a constant angle of 45.5^0. In this shot a PI controller was used and one can see that after a transient period of approximately 250ms the error signal reaches a constant zero value consistent with the presence if the integral term in the controller. On the right, simulated dynamics of the closed-loop feedback system using the @MATLAB's Simulink software package. In this simulation an analytic expression of the different transfer functions $G_i(s)$ has been used.

4. X3 Absorption studies on L-mode plasmas with mirror-angle real-time control

Results on the top-launch X3 absorption properties on L-mode plasma has been already reported in an earlier work [12] and a summary is presented in Fig.7. This study has been performed with the real-time control of the mirror angle and the measurement of the absorbed fraction is based on the measurement of the diamagnetic flux (DML) perturbation during a modulated portion of the injected rf power (full-power modulation of one gyrotron at 237Hz) [14]. The main conclusions of this study are: a) the real-time feedback is fully operational with L-mode plasmas, b) full single-pass absorption has been measured (DML) for central plasma densities lower than $5 \times 10^{19}\mathrm{m}^{-3}$.

At these plasma densities the calculated absorbed fraction (TORAY-GA), based on a maxwellian distribution function, is significantly lower than the measured one. The difference is to be associated with a suprathermal electron population created by the X3 itself. Evidence for this SEP is found on diagnostics sensitive to suprathermal electrons such as the high-field-side ECE[15] and a hard X-ray camera[16]. Similar results of an absorption enhancement in presence of a SEP have been obtained with a X3 low field side injection in presence of X2 CO-ECCD[17]. For a Maxwellian electron distribution function with a temperature of $T_e = 2keV$ and a characteristic width of the rf-beam ($w_0 = 33$ mm) the ratio $w_{res}/w_0 \simeq 1/2$. In presence of a SEP with a distribution assumed to be Maxwellian, depending on the temperature and density of the SEP, the ratio w^*_{res}/w_0 can become significantly larger than w_{res}/w_0 and therefore yield to an improved absorption. Without the presence of a SEP, as it is the case for H-mode plasmas, the ratio w_{res}/w_0 can be increased by decreasing w_0. This point will be discussed below.

5. X3 heating of H-mode plasmas

In recent experiments dedicated to heating of H-mode plasma it has been possible to reach nearly full single-pass absorption on a target plasma with a central density of $n_{e0} = 8. \times 10^{19}\mathrm{m}^{-3}$. In these experiments the real-time feedback on the mirror angle could not be used due to perturbations on the I_X signal associated with ELM induced density perturbations as well as fast density variation in ELM free periods occurring during the X3 rf pulse. It is planned to eliminate these effects by using, instead of the I_X signal ($I_X \sim n_e^2$), the T_{eX} signal which has no n_e dependence.

The temporal evolution of the relevant physical quantities of a typical shot are shown in Fig.8. As previously reported [12], with a total injected power of 1.35MW, an ELMy regime that is significantly different to ohmic/low-power-heating ELMy H-mode [18], has been found. This new regime of ELMy H-mode is highly reproducible and the measured absorbed X3 fraction, is in excess of 85% at central densities of $n_{e0} = 8. \times 10^{19}\mathrm{m}^{-3}$. The measured level of absorption is in good agreement with the value calculated with the ray-tracing code TORAY-GA. This result is consistent with the fact that no SEP is observed at these high densities.

The ratio between the ohmic power and the X3 absorbed power is typically $P_{ECH}/P_\Omega = 4-5$, which level is significantly higher than the preliminary results obtained with X3-heated H-modes [19]. The plasma stored energy is significantly increased to give a plasma β of 2.4%. Contrary to the case of L-mode plasmas, as shown in Fig.8, at these higher density levels a significant ion heating is observed which can be explained by both: a significantly higher coupling with the electrons (equipartition) together with an improved energy confinement during the X3 heated phase. Detailed analysis of these results is presently ongoing.

The measured electron density and temperature profiles (Thomson scattering) and the calculated absorption profiles (TORAY-GA) are shown in Fig.9. One notices that at the time of the X3 turn-on, the calculated absorbed fraction is approximately 30% and increases up to more than 90% once the stationary X3-heated phase is reached. The corresponding deposition profiles are shown on the right of Fig.9. During the stationary X3-heated-phase the deposition profile is more central compared to the one at the X3 turn-on.

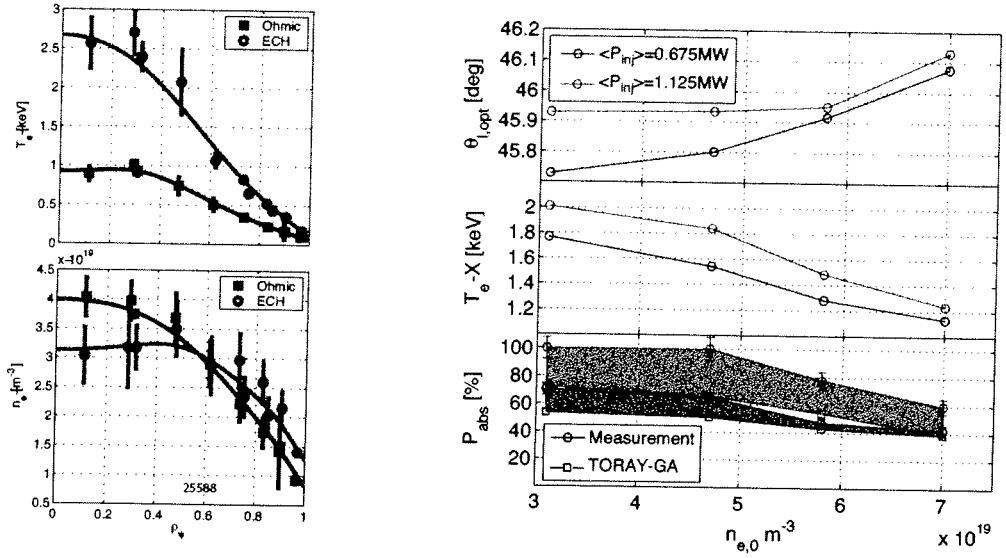

Figure 7. On the left, temperature and density profiles measure by Thomson scattering for a typical L-mode plasma with central temperature and density before the X3 rf pulse of $n_{e0} = 4.\times 10^{19}\mathrm{m}^{-3}$ and $T_{e0} = 0.9\mathrm{keV}$, respectively. The red curves correspond to the temperature and density profiles during the X3 heating. On the right is a summary the absorption studies on L-mode plasmas with two different injected rf power levels 0.675MW (blue curves) and 1.125MW (red curves). All the quantity are plotted versus the central electron density n_{e0} for both rf power levels. On top is the mirror angle θ_l, in the middle the electron temperature T_{eX} and on the bottom the absorbed fraction measured with the DML (open circles) and calculated with TORAY-GA (open squares). The target plasma used in these experiments have the following parameters: toroidal magnetic field, $B_T = 1.42\mathrm{T}$,major radius, $R_0 = 0.88\mathrm{m}$, minor radius. $a = 0.25\mathrm{m}$ elongation $\kappa = 1.53$, triangularity $\delta = 0.15$, plasma current: $I_p = 235kA$.

With a top launch configuration, by the nature of the heating scheme, nearly no control of the deposition profile is possible. However, at the plasma density and temperature reached in these H-mode X3-heated plasmas, the single-pass absorption of an X3 rf beam injected from the LFS would be larger than 55% (TORAY-GA). With such a level of absorption, a significant control of the deposition profile would be possible. In addition, with a LFS injection, the square dependence of the optical depth with temperature ($\tau_{X3,LFS} \sim T_e^2$) would bring the single pass absorption at even higher values. Motivated by these results we are presently studying the possibility to upgrade the installed X3 power on TCV by increasing the unit power of each existing gyrotron by approximately 30% ($\sim$ 600kW/gyrotron) and by adding a fourth gyrotron with a LFS injection.

6. Comparison between ray-tracing and beam tracing models

To assess the importance of diffraction effects on the X3 power absorption in the top launch configurations, a comparison between the beam tracing code ECWGB[20, 21] and the ray-tracing code TORAY-GA has been performed. The beam tracing code ECWGB can also be used as a ray-tracing code, by numerically turning-off diffraction effects.

Two main effects have motivated this study: first, the top-launch mirror has been designed such to have a waist (converging beam) approximately at the center of the vacuum vessel and, secondly, refraction effect can generate additional focussing inside the plasma. In this situation,

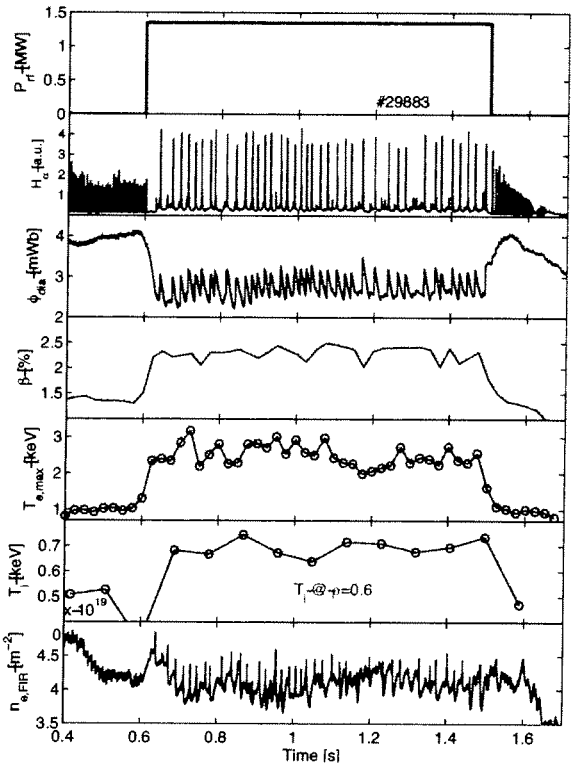

Figure 8. Relevant quantities for an H-mode heated plasma with an X3 injected power of 1.35MW. From top to bottom: rf power for X3, H_α emissivity, diamagnetic flux ϕ_{dia}, total plasma β (calculated with the equilibrium code (every 50ms) and constrained by the DML measurement), Thomson scattering peak electron temperature (every 17.5ms), ion temperature at $\rho = 0.6$ measured by active charge exchange spectroscopy, line integrated density. The target plasma used in these experiments have the following parameters: toroidal magnetic field, $B_T = 1.42$T, elongation $\kappa = 1.6$, triangularity $\delta = 0.55$, plasma current, $I_p = 380kA$.

the WKB approximation, on which the ray-tracing is based, might fail, and a more accurate model such as beam tracing might be necessary. With respect to the converging beam optics inside the plasma, the ray-tracing modeling of the rf beam in vacuum has been performed by imposing a ray distribution corresponding to a constant cylindrical cross section (no convergence) with a gaussian electric field distribution with a waist, $w_0 = 33$mm. This assumption is somehow unphysical, but very convenient, since, as it will be shown later, is a good approximation of a diffractive beam.

A first comparison between the two codes is shown in Fig.10. The ECWGB code, compared to TORAY-GA, uses a higher number of rays with a better homogeneity in the rays spatial distribution. In the top-launch configuration, the condition on ray homogeneity is very important as explained in [8]. In Fig.10 a) and b) 61 and 432 rays have been used respectively (only a subset are represented in Fig.10 b)). In Fig.10c) the total absorption (sum on all rays), is calculated along the central rays (in red in Fig. (a) and (b)) for each model and is represented in the $[\Psi_N, P_{abs}(\Psi_N)]$ plane. In this representation, the rf beam path in the plasma poloidal cross section is represented by the intersection of the central rays with the normalized flux surface, the rf beam enters the plasma at the point $P_{abs} = 0, \Psi_N = 1$, reaches the magnetic axis at $\Psi_N = 0$ and exits the plasma at $P_{abs,max}, \Psi_N = 1$. On notices that, for both models, the

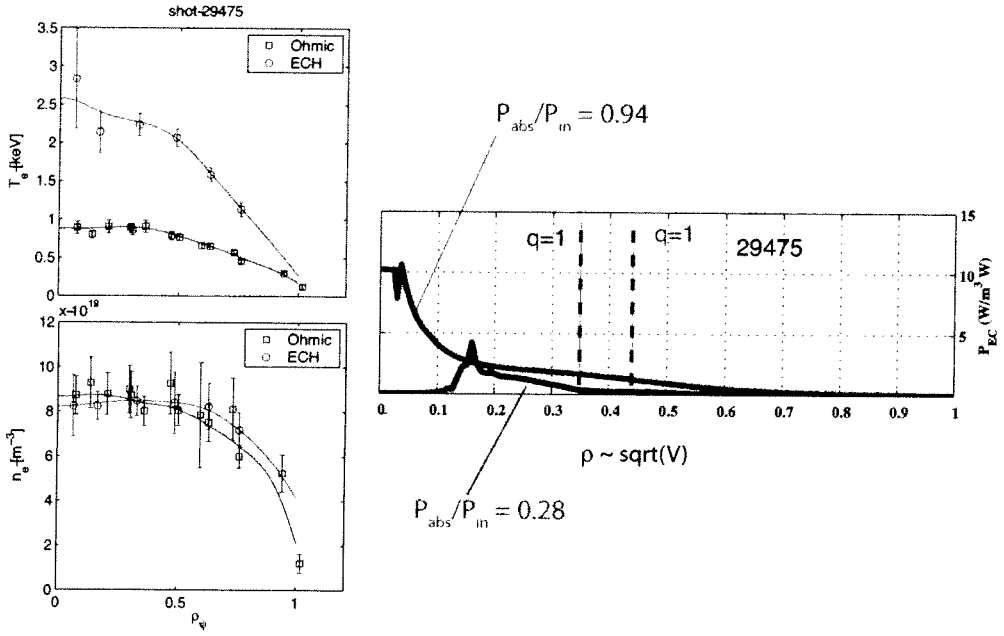

Figure 9. On the left, temperature (top-trace) and density profiles (bottom-trace) measured by Thomson scattering for a typical X3-heated H-mode plasma. In blue are represented profiles during the ohmic heated phase (before X3 turn-on) and in red profiles during the stationary phase of the X3 heating. On the right, with the same color coding, are the absorption profiles for the corresponding phases shown on the left.

absorption takes mainly place between the upper plasma edge and the plasma magnetic axis. We believe that the difference in global absorption shown in Fig.c) is to be associated to the different geometrical ray distribution. Further analysis on this aspect is presently ungoing.

The modeling with ECWGB has allowed to investigate the X3 top-launch injection for a beam optics with stronger focussing than the presently designed one which has, as mentioned earlier, a waist in electric field of $w_0 = 33$mm. Since, the ECWGB code has the flexibility to be used in "ray-tracing" or "beam tracing" mode, we have first checked the difference in calculated absorption for the two cases, where for the ray-tracing the rf beam has been approximated in vacuum as in TORAY-GA (constant cylindrical cross section with gaussian distribution). The rays distribution in vacuum are shown in Fig.11 left for the ray-tracing case and the beam tracing case.

The comparison between the ray-tracing and beam-tracing cases versus the focussing parameter w_0 is made in Fig.12. As it is shown on the left a), for the present waist of $w_0 = 33$mm, there is no difference between the two models and therefore justifies the cylindrical approximation made in TORAY-GA. At stronger focussing a relatively small difference between the two models is observed, but, more importantly, a significant increase of the absorbed power can be obtained. The increase of single-pass absorption with a stronger focussing is of particular interest for X3 heating of H-mode plasmas where the high density prevents the formation of a SEP. This is an important results since it would allow, by simply redesigning the launcher mirror, to significantly improve the single pass absorption.

In Fig.12 b), the absorption sensitivity versus mirror angle is shown for different waists. One observes that for stronger focussing the FWHM width $\delta\theta_l$ decreases, but remains well within the accuracy at which the real time control operates.

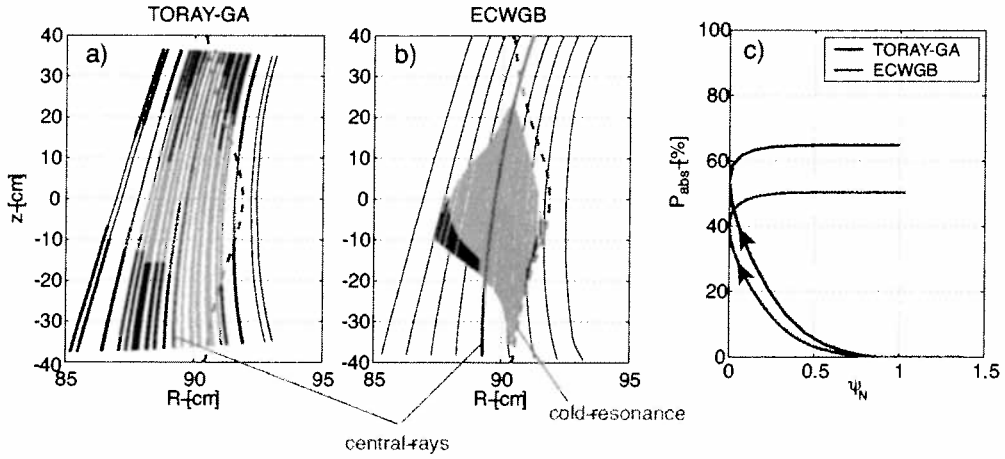

Figure 10. Fig. a) and b), ray trajectories calculated with TORAY-GA and ECWGB (with diffraction effects included), respectively. The only ray which must be exactly the same for the two codes is the central ray (in red in Fig. a and b). The calculated absorbed fraction on these specific central rays is the same, demonstrating that the absorption calculation is the same in the two codes. On (c), the global absorption is shown in red for the ECWGB code (diffraction effects included) and in red for TORAY-GA.

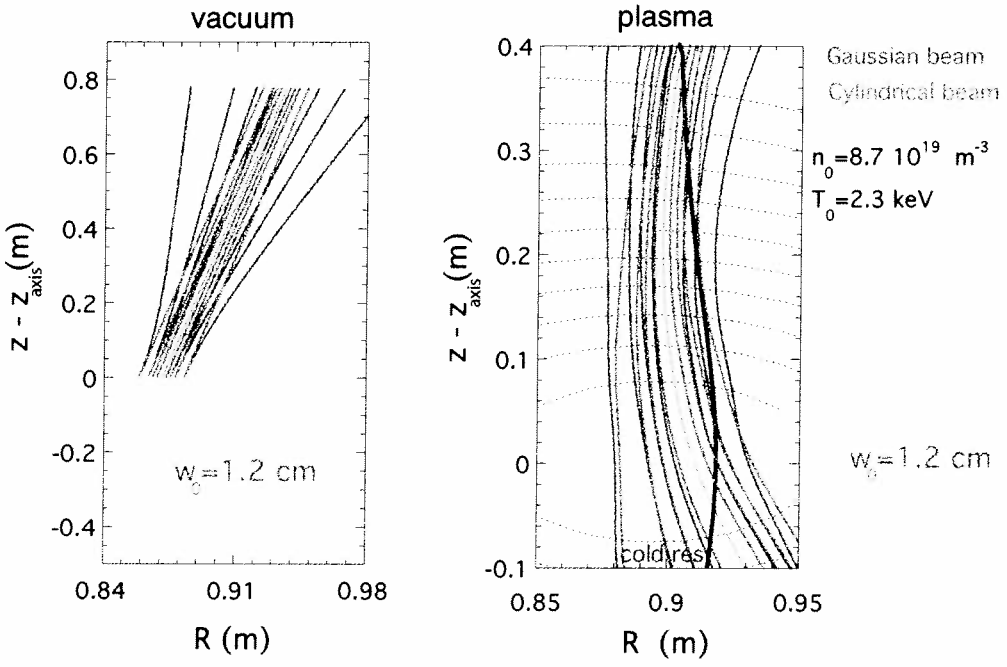

Figure 11. Ray trajectories for the ray-tracing case (cylindrical cross section without diffraction in orange) and the beam-tracing case (blue) used with ECBGW for a strongly focused beam with $w_0 = 12$mm. On the left are the corresponding ray trajectories in vacuum. On the right with a plasma of central temperature and densities of $T_{e0} = 2.3$keV and $n_{e0} = 8.7 \times 10^{19}\mathrm{m}^{-3}$. The density and temperature profiles correspond to the profiles of the L-mode plasma shown in Fig.7 left.

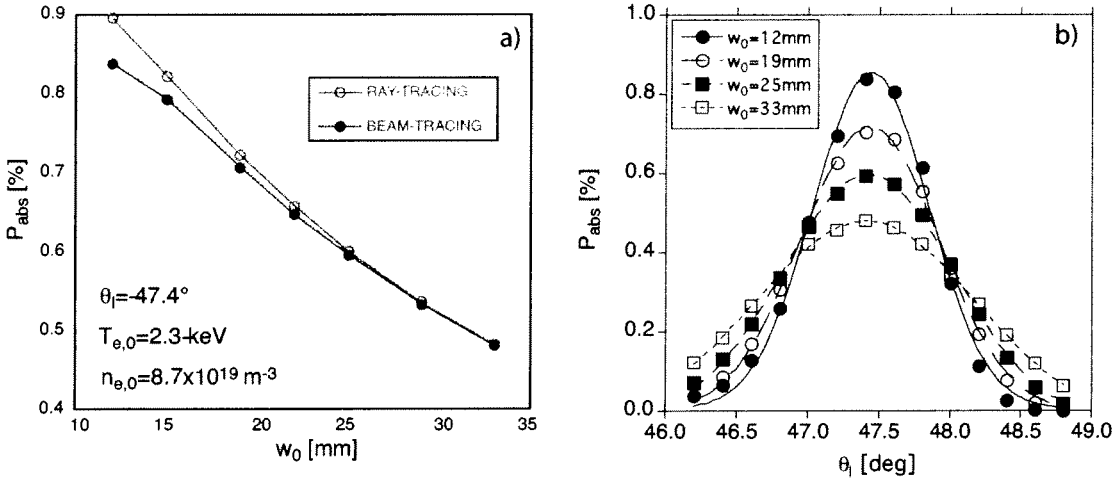

Figure 12. Comparison with ECWGB of the beam-tracing model and the ray tracing model. Fig. a) on the left shows a comparison of the two models (in blue ray-tracing, in red beam-tracing) where the absorbed fraction is plotted against the waist w_0 with the mirror angle at the optimum value $\theta_l = 47.4^o$. The central electron density and temperature as well as the corresponding profile are the same as in Fig.11 and the present waist is $w_0 = 33$mm. On the right, Fig. b), the absorbed fraction versus mirror angle is calculated with the beam tracing model for various waists w_0.

7. Conclusions

A top-launch X3 ECH system with a total injected power of 1.35MW has been installed on TCV in order to heat high density plasmas. For this launching configuration, the numerically predicted and experimentally observed strong dependence of the X3 absorption on the mirror angle has motivated the development of a real-time control of the mirror angle. This real-time control is based on a mirror modulation technique which allows to generate via a synchronous demodulator an error signal proportional to the derivative of the plasma response versus mirror angle. Stationary control of the mirror have been achieved with a PI controller. Future plans include the implementation of such a system on the X2 launchers for EBW experiments and/or real time control of MHD activity such as sawteeth. This system has been successfully tested and has allowed to perform extensive absorption studies in L-mode plasmas. With a total injected power of 1.35MW, full-single pass-absorption has been reached with a significant fraction of the power absorbed on a suprathermal electron population generated by the X3 wave itself. With 1.35MW of X3 injected power we have demonstrated the accessibility to an ELMy regime that is significantly different to ohmic/low-power-heating ELMy H-modes.

Comparisons between the linear ray-tracing code TORAY-GA and the beam-tracing code ECWGB has allowed to validate the cylindrical cross section approximation used in TORAY-GA for the presently used launcher optics ($w_0 = 33$mm). With a stronger focussing of the rf beam ($w_0 < 33$mm), ECWGB predicts a significantly higher single-pass absorption. Plans to modify the top-launcher mirror with a stronger focussing are presently underway.

8. Acknowledgments

This work was partly supported by the Swiss National Science Foundation.

[1] R. Prater, Heating and current drive by electron cyclotron waves, Phys. Plasmas **11**(5) (2004), 2349–2376.

[2] M. Maraschek et al., in Fusion Energy 2004 (Proc. 20th Int. Conf. Vilamoura, 2004) (Vienna: IAEA) CD-ROM file EX/7-2 and http://www-naweb.iaea.org/napc/physics/fec/fec2004/datasets/index.html
[3] C.C Petty et al., in Fusion Energy 2004 (Proc. 20th Int. Conf. Vilamoura, 2004) (Vienna: IAEA) CD-ROM file EX/7-3 and http://www-naweb.iaea.org/napc/physics/fec/fec2004/datasets/index.html
[4] K. Nagasaki et al., in Fusion Energy 2004 (Proc. 20th Int. Conf. Vilamoura, 2004) (Vienna: IAEA) CD-ROM file EX/7-3 and http://www-naweb.iaea.org/napc/physics/fec/fec2004/datasets/index.html
[5] C. Angioni, T.P. Goodman, M.A. Henderson, O. Sauter, Effects of localized electron heating and current drive on the sawtooth period, Nucl. Fusion **43** (2003), 455.
[6] M.A. Henderson, Y. Camenen, S. Coda, T.P. Goodman, P. Nikkola, A. Pochelon, and O. Sauter, Rapid and Localized Electron Internal-Transport-Barrier Formation During Shear Inversion in Fully Noninductive TCV Discharges, Phys. Rev. Lett. **93**, 215001 (2004).
[7] H.P. Laqua, W7-AS Team, Electron Bernstein wave heating in fusion plasmas, Proceedings of the 15th Topical Conference on Radio Frequency Power in Plasmas, Moran, Wyoming, edited by C.B. Forest (AIP, New York, 2003), p. 15.
[8] G. Arnoux, S. Alberti, L.Porte, E.Nelson-Melby, J.P. Hogge and the TCV Team, Third harmonic X-mode absorption in a top-launch configuration on the TCV tokamak, Plasma Phys. Control. Fusion, **47** (2005), 295–314.
[9] T. Goodmann et al, Design and installation of the electron cyclotron wave system for the TCV tokamak, Fusion Technology (Proc. of 19th Symp. Lisbon 1996), North-Holland, Amsterdam (1997), 565.
[10] J.P. Hogge, S. Alberti, L.Porte and G.Arnoux, Preliminary results of top launch third harmonic X-mode electron cyclotron heating in the TCV tokamak, Nucl. Fusion, **43** (2003), 1353.
[11] R. Chavan, M. Henderson and F.Sanchez, E.Nelson-Melby, J.P. Hogge and the TCV Team, Third harmonic X-mode absorption in a top-launch configuration on the TCV tokamak, Plasma Phys. Control. Fusion, **47** (2005), 295–314.
[12] S. Alberti, G.Arnoux, L.Porte, J.-P.Hogge, B.Marlétaz, P.Marmillod, S.Nowak, Y.Martin and the TCV Team, Third-harmonic, top-launch, ECRH experiments on TCV Tokamak. Accepted for publication in Nuclear Fusion.
[13] J. Kiraly, et al., Nucl. Fusion, **27** (1987), 397.
[14] A. Manini, J.-M. Moret, S. Alberti, T.P. Goodman and M.A. Henderson, Modulated ECH power absorption measurements using a diamagnetic loop in the TCV tokamak, Plasma Phys. Control. Fusion, **44** (2002), 139-157.
[15] P.Blanchard, S. Alberti, S. Coda, H.Weisen, P.Nikkola and I.Klimanov, High Field side measurements of non-thermal electron cyclotron emission on TCV plasmas with ECH and ECCD, Plasma Phys. Control. Fusion, **44** (2002), 2231–2249.
[16] S. Coda,S. Alberti, P.Blanchard, T.P. Goodman, M.A. Henderson, P. Nikkola, Y. Peysson, and O. Sauter, Electron cyclotron current drive and suprathermal electron dynamics in the TCV Tokamak, Nucl. Fusion **43** (2003), 1361.
[17] S. Alberti, T.P. Goodman, M.A. Henderson, A. Manini, J.-M. Moret, P. Gomez, P. Blanchard, S. Coda, O. Sauter, Y. Peysson and the TCV Team, Full Absorption of third harmonic ECH in TCV tokamak plasmas in the presence of second harmonic ECCD, Nucl. Fusion **42** (2002), 42.
[18] Y. Martin and TCV Team, Accessibility and properties of ELMy H-mode and ITB plasmas in TCV, Plasma Phys. Control. Fusion, **45** (2003), A351-A365
[19] L.Porte et al., in Fusion Energy 2002 (Proc. 19th Int. Conf. Lyon, 2002) (Vienna: IAEA) CD-ROM file EX/P5-15 and http://www.iaea.org/programmes/ripc/physics/fec2002/html/fec2002.html
[20] S. Nowak and A. Orefice, Three-dimensional propagation and absorption of high-frequency Gaussian beams in magnetoactive plasmas, Phys. Plasmas **1**(5) (1994), 1242–1250.
[21] D. Farina, S. Nowak and G. Ramponi, ECWGB: a beam tracing code for EC heating and current drive ,IFP-CNR Internal Report FP 03/6, October 2003, http://www.ifp.cnr.it/publications/2003/FP03-06.pdf

A Frictionless Steering Mechanism for the Front Steering ECCD ITER Upper Port Launcher

R. Chavan[1], M.A. Henderson, F. Sanchez

CRPP, Association EURATOM- Confédération Suisse, EPFL, CH-1015 Lausanne, Switzerland

rene.chavan@epfl.ch

Abstract. A FS launcher is being designed for the ITER upper port, which offers enhanced physics performance over the RS launcher. A two mirror system is used to decouple the focusing and steering aspects of the launcher and provide a relatively small beam waist (<20mm) projected far into the plasma (>1.6m from the steering mirror). The resulting NTM stabilization efficiency (maximum CD density divided by the local bootstrap current > 1.6) is above marginal for the q=2 and 3/2 rational flux surfaces of the relevent ITER equilibria (scenarios 2, 3a and 5) and a factor of ~3 relative to an equivalent RS launcher. The performance of the FS launcher strongly depends on the reliability of the steering mechanism, which is used to rotate the plasma facing steering mirror. CRPP has designed a frictionless steering mechanism assembled in a compact cartridge capable of up to ±10° rotation (corresponding to a poloidal steering range of up to ±20° for the microwave beam around a fixed axis of rotation) that offers a high operation reliability despite the close proximity to the thermal and neutron flux coming from the ITER plasma.

1. Introduction

The purpose of the ITER electron cyclotron resonance heating (ECRH) upper port launcher will be to drive current locally inside a q=3/2 or 2 island in order to stabilize the neoclassical tearing mode (NTM). Unfortunately, the uncertainties due to our limited experience using ECCD for NTM stabilization magnified by extrapolation to ITER, results in a relatively large range of current drive densities and injection angles that may be needed on ITER. Although the remote steering (RS) launcher design [1] offers the advantage of not requiring moving parts within the vessel vacuum boundary (far from the thermal and nuclear radiation of the plasma), it has a angular range of ±12° limited by the beam transmission properties of the square corrugated waveguide and a relatively broad beam spot size at the resonance surface. The angular range is decreased (~ ±10°) due to additional focusing affects of the plasma facing mirror after the waveguide aperture. Whereas, the front steering (FS) launcher offers an extended angular range (~ ±20°) and a narrower spot size at the resonance. A FS launcher [2] is already being planned for the equatorial port where thermal and neutron radiation fluxes are, in fact, higher than at the upper port. In light of this, an alternative FS launcher for application on the ITER upper port is proposed [3, 4]. Although the standard ITER design value is currently 1 MW per beam, the launcher is capable of injecting over 16MW per port, assuming eight beams of 2MW and in anticipation of the the 2MW gyrotron under development within the European Community [10]. A two mirror system (1 focusing-fixed and 1 flat-steering) for focusing and

[1] To whom any correspondence should be addressed

redirecting the beam towards the q=3/2 or 2 flux surfaces for all envisioned plasma equilibria is used. This paper provides a brief description of the envisioned optical front mirror steering mechanism followed by a conclusion.

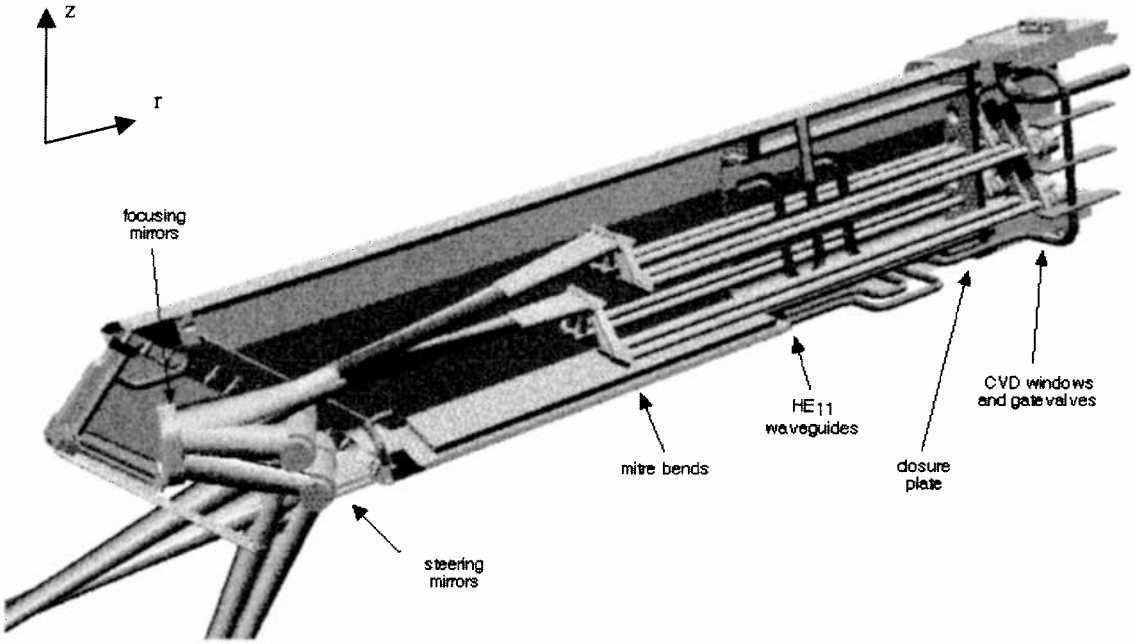

FIGURE 1. A poiloidal/radial section through the upper port plug, showing the simplified beam path, with internal shielding elements removed.

A simplified poloidal section view of the current FS launcher design is shown in figure 1. Eight circular waveguides enter at the port entrance on the right, with the waveguides arranged in two rows of four. A miter bend 'dog-leg' assembly is used to angle the 8 beams (both in toroidal and poloidal directions) to one single focusing mirror, the incident beams partially overlap in both toroidal and poloidal directions. The reflected beams are then directed downward to two separate flat steering mirrors, which redirect the beams into the plasma with a toridal injection angle. Since the beams are allowed to expand from the waveguide aperture, they can be refocused to a narrow waist far into the plasma (>1.6m after steering mirror). The angular rotation of the steering mirror (±6.5°) provides access along the resonance layer from Z_{res} = 1.8 to 3.6m.

2. Steering Mechanism requirements

The steering requirement imposed by NTM physics, taking into account the rather unfavourable location with high z elevation of the upper ports, is for a beam rotation of ±13°, equivalent to mirror rotation of ±6.5°. ITER relevant requirements include the sustaining of continous thermal and nuclear radiation, to withstand electromagnetically induced forces during disruptions, to provide accurate angular positioning with an error of less than 0.2°, the compatibility with water circuit interfaces (cooling, baking) and the compatibility with remote handling tools and procedures. The steering system has to work reliably and guarantee fail-safe operation avoiding major interference with the tokamak activity.

Additional requirements have been formulated by CRPP, they include a preferably frictionless and backlash-free mechanical transmission and actuation system (to avoid bearings, bushings, push rods). In order to fulfill extended physics requirements to include ELM control and CD [4-6], the beam steering range should be increased to ± 20° (± 10° at steering mirror). Optimal beam focusing at

deposition location allows to increase the overall peformance and reliability margin of the ECCD through higher j_{CD}/j_{BS} values, since failure of a number of beam lines can be tolerated while still achieving full NTM stabilization. The j_{CD} deposition will be measured relative to the rational flux surface (q=2 or 3/2) in the plasma using diagnostics systems such as ECE for real time feedback control of the mirror launcher angles, thus bypassing the need for an angular measuring and feedback system on the steering mirror. However, the angular position of the mirror may be optionally monitored using, for example, rotational variable capacitor or an opto-encoder.

3. Description of steering mechanism

In order to demonstrate the feasibility of a front steering EC antenna system which accomodates the limited space constraints within the upper port plug of the present ITER reference design and yet offer full beam steering capability over an angular range of +/- 20°, a robust steering mechanism with a reduced number of components is described. The FS launchers on existing tokamaks have been hindered when the steering mechanism grips. Experience with mechanical assemblies involving ball bearings, bushings, push/pull rods and various types of linkages and cams operating in UHV conditions have shown to be insufficiently reliable and frequently subject to excessive wear or gripping. Tribological failures are the main cause for premature break down of systems where friction, wear and the absence of lubrication of interacting surfaces in relative motion are dominant. Movements of small amplitude and high frequency are exacerbating tribological problems, as does the potential presence of metallic and ceramic dust particles and sputtered surface contaminants. These are the justifications for the use of elastically compliant concepts, which eliminate friction, backlash, clearance. The proposed design offers sufficient stiffness and is intrinsically play-free and thus avoids backlash and stick-slip phenomena.

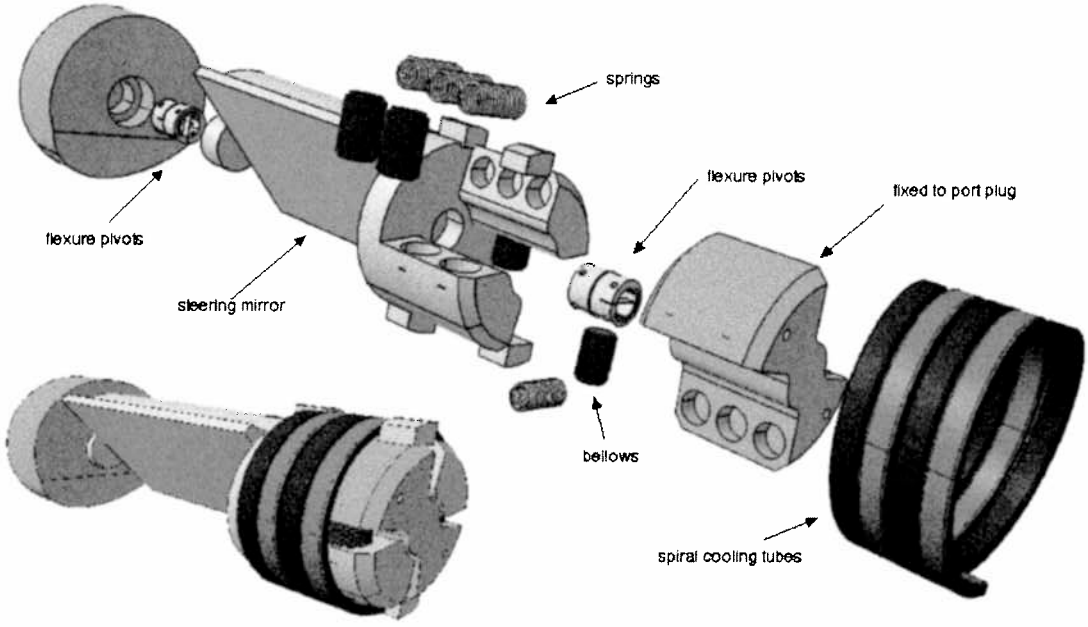

FIGURE 2. Exploded view of the main elements of the front mirror and the steering mechanism (below) and assembly view (top).

As shown in figure 2, a set of elastically compliant flexure pivots replace the traditional ball bearings in centering and guiding the rotation of the steering mirror. Made of just five machined parts in it's current implementation, it utilizes a orthogonal set of three flat spring blades in a typically

cylindrical cartridge housing. The main advantage of the flexure pivot lies in frictionless and backlash free operation. There is no need for static preloading to remove clearance. By choosing the appropriate material combining good elastic properties under cyclic loading conditions and simultaneous neutron irradiation, as those expected in the region behind the first wall shielding, the flexure pivot provides precise and repeatable rotation with a very small excentricity over a large number of cycles.

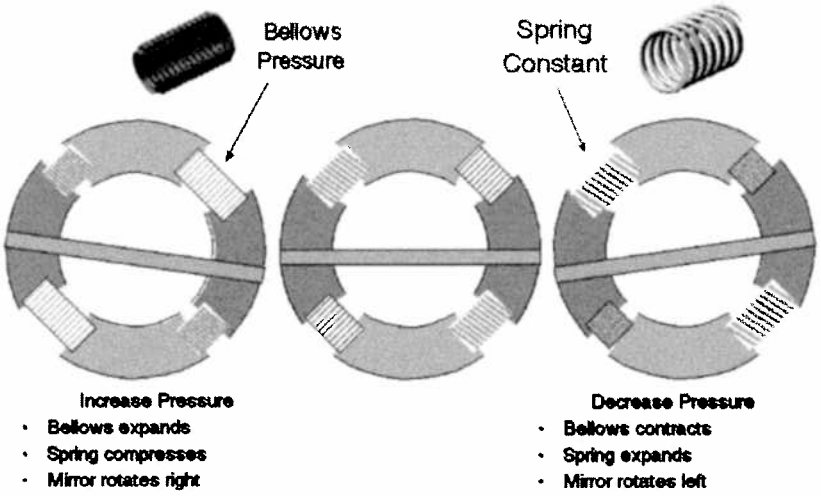

FIGURE 3. A sketch on the pneumatic principle of the actuator.

The mirror movement is achieved by a helium gas actuator assembly replacing the generally used push-pull rods. The mirror rotation is controlled by the helium pressure in the bellows counteracted by a set of compressive springs, as shown schematically in figure 3. The pressure in the seamless bellows is controlled via a single small bore gas feed line by a piezoelectric servo valve located outside the vessel vacuum behind the closure plate. A magnetically driven servo valve could be used with appropriate electromagnetic shielding or at a location where the magnetic field would be acceptably low. Two arms extend past the edge of the mirror, and are positioned symmetric about the mirror axis. Each arm passes between a set of tangentially arranged bellows and preloaded compressive springs. The mirror is rotated when the arms are moved by either increasing or decreasing the pressure in the bellows, counteracting the recalling torque imposed by the compressed springs. The complete system is integrated into a cartridge type construction, with all static forces and torques being fully balanced within and thus requiring no structural link to the embedding neutron shielding and plug structure other than the centering housings interfacing with the flexure pivots. The mirror can be controlled on a sufficiently rapid time scale with a calculated time constant of typically 20 ms, into which the time delay caused by the long helium feeding pipe is included. This simple servovalve system with pressure feedback control, as shown in figure 4, works on the linear relationship between bellow pressure and spring compression proportional to the steering angle. Although rotation angle measurement is not necessarily required as the actual orientation of the beams can be detected by indirect means via the invessel diagnostic systems with pulsed beam modulation or small angular range scanning, systems using a variable capacitor integrated into the rotor [7] or a optical encoder with optical fiber [8] are under consideration.

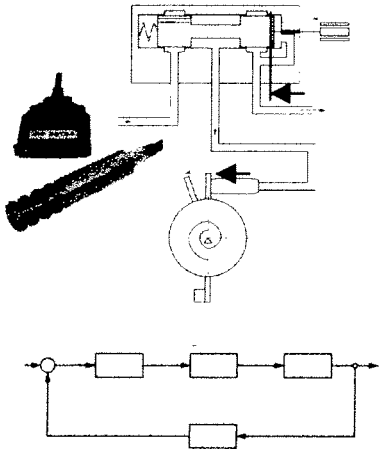

FIGURE 4. Linear relationship between bellow pressure and spring compression proportional to the steering angle allows for servovalve control with pressure feedback.

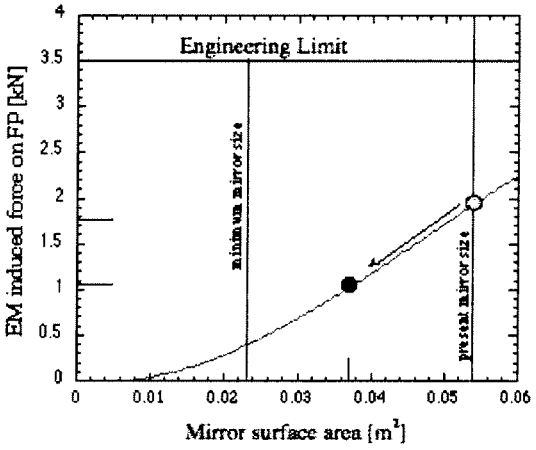

FIGURE 5. Possible reduction of EM induced forces by further reducing the steering mirror size

The cooling water removes the surface heat generated through ohmic losses of the reflected beam at the mirror surface and the volume heat from neutron absorption in all massive components. The water circulates through the static and the rotating parts of the front steering cardridge. The fluid paths are optimized for keeping the lowest possible temperature at the reflecting mirror surface while minmizing thermal gradients and consequent distortions of the mirror rotor, which would degrade the beam quality. The use of water feeding and fatigue sensitive and thus less reliable bellows or corrugated tubes to circulate the water in the rotor is avoided by winding a pair of spiral pipes around the section of the mirror housing the actuators and springs, welded between the mirror/rotor and the stator parts.

4. Critical elements

The steering mechanism is the critical component of the FS design and a failure of one steering mechanism would render four mm-wave beams unavailable for NTM stabilization applications. It is important to note that a failed steering mechanism can only be replaced during a normal tokamak opening. However, half of the total number of FS steering mechanisms could fail and still provide sufficient NTM stabilization performance (8 beam/3 port configuration).

The EM forces related to the induced currents during a disruption were estimated for the steering mirror in the worst configuration and assuming no shielding effect from the port wall, dB_P/dt=25T/s (plasma current 17.85MA and linear current decay time 0.04s [11]) and B_T=5.0T. The latest values given for disruptions of type III [12] will be accounted for in the final design of the mirror and flexure pivot assembly. The mirror dimensions are 305mm (toroidal), 210mm (poloidal) and >0.5mm (copper thickness), with the mirror made from steel, while electrical insulation breaks are introduced on the back side limiting the effective thickness. The resulting net torque on the mirror is 590Nm, resulting in a force of <2 kN per flexure pivot (a flexure pivot is positioned on each side of steering mirror). The flexure pivots are capable of supporting up to 3.5kN at full steering angle for the present configuration. The induced EM forces will actually be less than 45% of the flexure pivot force limit once the shielding effect of the port wall is taken into consideration, as shown in *Fig. 5.*

The flexure pivots are made of a titanium alloy (Ti6Al4V or Ti5Al2.5Sn) capable of withstanding the neutron fluxes and induced stresses during plasma disruption and offering the appropriate tensile and fatigue behavior under irradiation. The stress versus strain curves and fatigue life have been determined for irradiated samples at 350 C in vacuum [9], with yield strength reaching 800 MPa, as shown in Fig. 6. The desired design values for the flexure pivot and similar elastically deformed componenets are stress below 200 MPa and strain below 0.5 %, while strain of typically 1% results in fatigue life of at least 10'000 cycles. The proposed stress/strain values are comparable to those found in the flexible mechanical attachments used to hold the first wall blanket shield modules, made of Ti6Al4V [8].

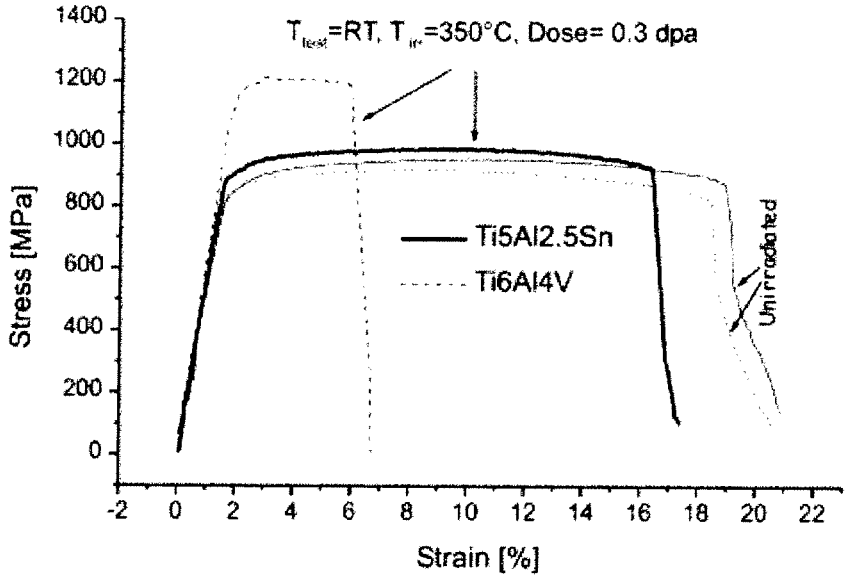

FIGURE 6. Stress / strain curve for irradiated titanium alloy samples [9].

Fatigue cycling, thermomechanical and hydrostatic loads under simultaneous neutron flux exposure are equally critical in structural elements such as the pneumatic bellow actuator, the compressive spring and the cooling water feed coil. Concepts aimed at reducing mechanical stress in the spiral coolant feeds, such as tubes with rectangular rather than circular cross section, are under investigation. Particular attention is given to the welded connexions of the pipework. A coiled cooling tube with either a single or double wall is envisioned to provide method of water leak testing.

The spot sizes on both the focusing and steering mirrors are relatively large (65.0mm and ~50.0mm respectively) and, as a result, the peak power density is reduced significantly despite the partially overlap of multiple 2.0MW beams. The maximum power density reaches ~3.4MW/m^2, which occurs on the lower steering mirror. Absorbed power is calculated assuming circular polarization and an absorption coefficient of 0.005 to account for increased temperature, surface roughness and surface impurity effects. The relatively low power density on the FS steering mirror offers the possibility of using non-copper reflective material such as beryllium or tungsten to avoid copper sputtering into the plasma or reduce surface erosion.

5. Mechanical and hydraulic fail safe operation

The FS system is designed to provide mechanical and hydraulic fail safe operation. For example, the steering mirrors use dedicated cooling circuits, which can be isolated and evacuated if a water leak is detected. The quantity of water released into the torus vacuum is minimized. Furthermore a passive

cooling scheme to remove heat generated by absorbed neutrons in case of failure of the water cooling is necessary and foreseen, where radiative and conductive heat fluxes are sufficient to maintain the steering mirror components at a reasonably low temperature for the remaining time of tokamak operation, until replacement of the FS assembly is possible.

6. Conclusion

Despite the stringent geometrical, thermo-mechanical, nuclear and RF requirements, a FS launcher system based on an invessel steering mechanism appears feasible. To achieve the sufficient reliability and fail-safe operation of the FS steering mechanism, frictionless elements with determined properties of elastic compliance systematically replace traditional components where friction and rolling contacts between surfaces limit the functional lifetime inside the torus vacuum. The backlash and clearance free flexure pivot replacing the ball bearing is typically made of an ITER compliant titanium alloy. Integrating the pneumatic actuator principle based on pressure controlled helium into a self contained cartridge type assembly replaces external push-pull rods. The addition of spiral cooling pipes to avoid bellow coolant feeds makes the launcher hydraulically and mechanically fail safe, where tokamak operation is maintained even after the failure of a front mirror assembly. The steering mechanism is designed to support at least two times the electromagnetically induced loads expected during a VDE in ITER. The realized design features include a beam scanning range of ±20°.

The complete engineering study is ongoing and will be finalized with the production of manufacturing drawings, the construction and finally the test of a prototype under simulated ITER conditions, including low power RF beam tests of the optical system.

7. Acknowledgement

This work was supported in part by the Swiss National Science Foundation and the European Fusion Development Agreement under the EFDA Technology Programme (contract TW4-TPHE-ECHULB1).

References

[1] Verhoeven A G A 2004 *Design of the mm-wave system of the ITER upper port launcher* Proc. 13th ECE & ECH, Nizhny Novograd, http://www.ec13.iapras.ru/on-line-papers.htm

[2] Takahashi K, Imai T, Kobayashi N, Sakamoto K, Kasugai A, Hayakawa A, Mori S and Mohri K 2005 Fusion Science and Technology **47** 1.

[3] Chavan R, Henderson M A and Sanchez F *An alternative ECRH Front Steering Launcher for the ITER Upper Port*, accepted for publication in Fusion Engineering and Design.

[4] Henderson M A *et al.*, *The Front Steering Launcher Ddesign for the ITER ECRH Upper Port*, accepted for publication in JCPS IAEA-TM on ITER/ECRH.

[5] H. Zohm, "The ITER ECRH upper launcher - physics goals and design requirements", Proc. 13th ECE & ECH, Nizhny Novograd (2004), http://www.ec13.iapras.ru/on-line-papers.htm

[6] Zohm H, Heidinger R, Henderson M, Poli E, Ramponi G, Saibene G, Verhoeven A G A 2005 *Comparison of the performance of different options for the ITER ECRH Upper Launcher,* submitted JCPS IAEA-TM on ITER/ECRH.

[7] Prater R 2005 General Atomics, Private communication.

[8] A. Coletti et al. 2003 *AM laser system (IVVS) for the ITER in vessel viewing and ranging* Fusion Engineering and Design **69** 169-175.

[9] Marmy P. et al., 2001 *Impact of irradiation on the tensile and fatigue properties of two titanium alloys* Journal of Nuclear Materials **296** 155-164.

[10] Hogge J.P. et al., *Development of a 2-MW, CW Coaxial Gyrotron at 170 GHz and Test Facility for ITER*, submitted JCPS IAEA-TM on ITER/ECRH.

[11] ITER DDD1.6 Blanket Electromagnetic Analysis, G 16 DDD 35 R0.1.

[12] ITER Load Specifications, ITER_D_222QGL v3.0.

The Front Steering Launcher Design for the ITER ECRH Upper Port

M.A. Henderson[1,6], R. Chavan[1], R. Heidinger[2], P. Nikkola[1], G. Ramponi[3], G. Saibene[4], F. Sanchez[1], O. Sauter[1], A. Serikov[2], H. Zohm[5]

[1] CRPP, Association EURATOM- Confédération Suisse, EPFL, CH-1015 Lausanne, Switzerland
[2] Forschungszentrum Karlsruhe, Association FZK - EURATOM, D-76021 Karlsruhe, Germany
[3] Istituto di Fisica del Plasma, EURATOM- ENEA-CNR Association, 20125 Milano, Italy
[4] EFDA Close Support Unit, Boltzmannstrasse 2, D-85748 Garching, Germany
[5] IPP-Garching, Max-Planck-Institut für Plasmaphysik, D-85748 Garching, Germany

mark.henderson@epfl.ch

Abstract. The ECRH ITER upper port antenna's role is to stabilize the neoclassical tearing mode (NTM) on either the q=2 or 3/2 rational flux surfaces, which requires a narrow current deposition profile (j_{CD}) over a wide range along the resonance surfaces. The width of j_{CD} should be equivalent to the marginal island width to fully stabilise the NTM. Two antenna concepts are under consideration for the upper port launcher: front steering (FS) and remote steering (RS). The FS launcher decouples the steering and focusing aspects using a two mirror system (one focusing and one steering), achieving a wider steering range and higher current density for NTM stabilisation than required by ITER, offering a threefold increase in NTM stabilization efficiency over the RS launcher. The improved physics performance has motivated the further design study of the FS launcher aiming toward a build to print launcher. The present design is compatible with ≥2.0MW CW operation and 8 beams per port plug. A frictionless backlash-free system is envisioned for the steering mechanism. An overview of the launcher design, the calculated physics performance and the possibility of using the upper port launcher for extended physics applications (beyond NTM stabilisation) are discussed.

1. Introduction

The purpose of the ITER electron cyclotron resonance heating (ECRH) upper port antenna (or launcher) will be to drive current (ECCD) locally inside the island which forms on the q=3/2 or 2 rational magnetic flux surfaces after the onset of the neoclassical tearing mode (NTM) [1-4]. In order to fully stabilize the NTMs, the launcher should be capable of steering the ECCD current deposition profile (j_{CD}) across the resonance surface over the range in which the q=3/2 and 2 surfaces are found, for the various plasma equilibria susceptible to the onset of NTMs [5], as shown in figure 1. Also, j_{CD} must be narrow relative to the marginal island width and its amplitude greater than that of the bootstrap current (j_{BS}) found outside the island in order to effectively stabilize the NTM [6], as

[6] To whom any correspondence should be addressed

illustrated in figure 2. The ratio of these two currents, $\max(j_{CD})/j_{BS}$, provides an NTM stabilisation figure of merit (η_{NTM}). The physics objective for the launcher is to achieve $\eta_{NTM} \geq 1.2$ for the various relevant plasma equilibria that are susceptible to NTMs (equilibria 2, 3a and 5) [5].

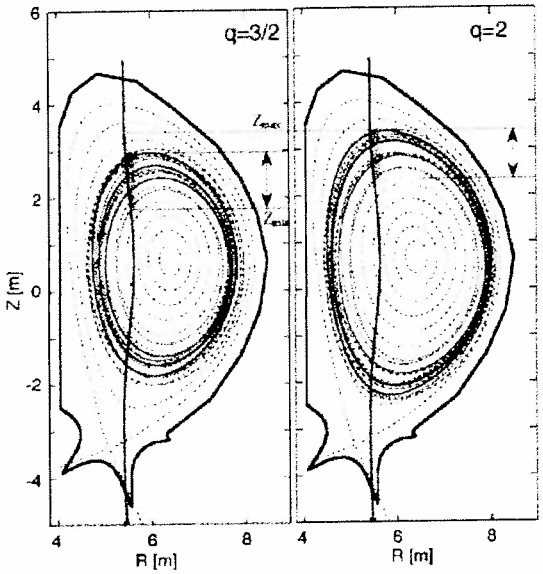

FIGURE 1. The q=2 and 3/2 flux surfaces susceptible to the NTM, with Z_{min} and Z_{max} indicating the lower and upper region in the plasma that the launcher must access along the resonance surface (vertical line) [5].

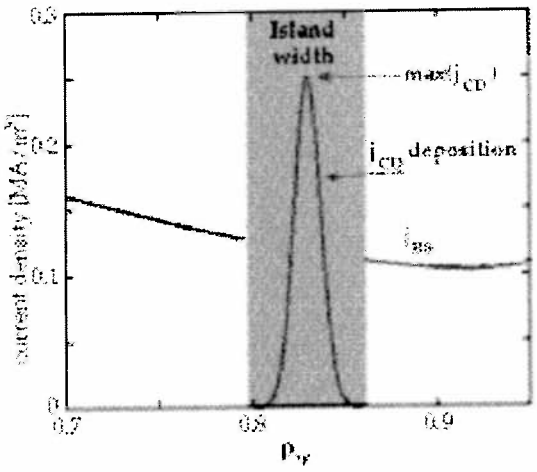

FIGURE 2. Illustration of the current density profile relative to the bootstrap current, the NTM stabilization efficiency, η_{NTM}, is given by $\max(j_{CD})/j_{BS}$.

The European Fusion Development Agreement (EFDA) is currently in the process of developing two launcher designs in parallel: remote steering (RS) and front steering (FS) launchers. The RS concept [6] offers the advantage of not requiring moving parts within the vessel vacuum boundary (far from the thermal and nuclear radiation of the plasma). However, it has a limited angular range ($\leq \pm 12^{\circ}$) and projects a relatively broad beam spot size (>55mm) at the resonance surface [8]. By contrast, the FS launcher offers an extended angular range (up to $\pm 24^{\circ}$) and projects a much narrower spot size on the resonance surface [9,10], but requires a rotatable mirror near the plasma. EFDA's strategy is to investigate the two launcher systems, comparing their physics performance, engineering reliability and costs, with the ultimate aim of providing the optimum launching system for the ITER upper port.

This paper will concentrate on the FS launcher design and its expected performance for NTM stabilization. First the overall launcher design is described in section 2. In section 3 the estimated NTM stabilization efficiency is given based on the beam tracing code ECWGB [11]. In section 4 the potential for extended physics applications using the FS launcher will be discussed followed by a conclusion in section 5.

2. FS launcher design

A simplified poloidal view of the FS launcher design is shown in figure 3. Eight circular waveguides enter at the port entrance on the right, with the waveguides arranged in two rows of four. Before the closure plate there is an in-line carbon vapor deposition (CVD) diamond window [12], which provides a tritium barrier preventing any tritium from penetrating into the evacuated waveguide transmission line and traveling up to the gyrotron. An in-line all-metal gate valve is placed on the plasma side of the

CVD window (see figure 3). The gatevalve offers a secondary level of protection, which closes in case the CVD window leaks or is broken [13]. The gatevalve can be purchased with an auxiliary port installed on the gatevalve body, which provides pumping access to the inner vacuum region between the valve and window. In addition, this auxiliary port on the gatevalve can be used to test the vacuum integrity of the CVD window by leaking helium into the auxiliary port and monitoring for helium in the transmission line's in-line pumping station on the gyrotron side of the window. Both the window and gatevalve will be held rigidly to the port plug. The aluminum waveguide on the gyrotron side of the CVD window (not shown in figure 3) will bend (elastically) compensating for the displacement of the torus during thermal cycles or disruption events [13].

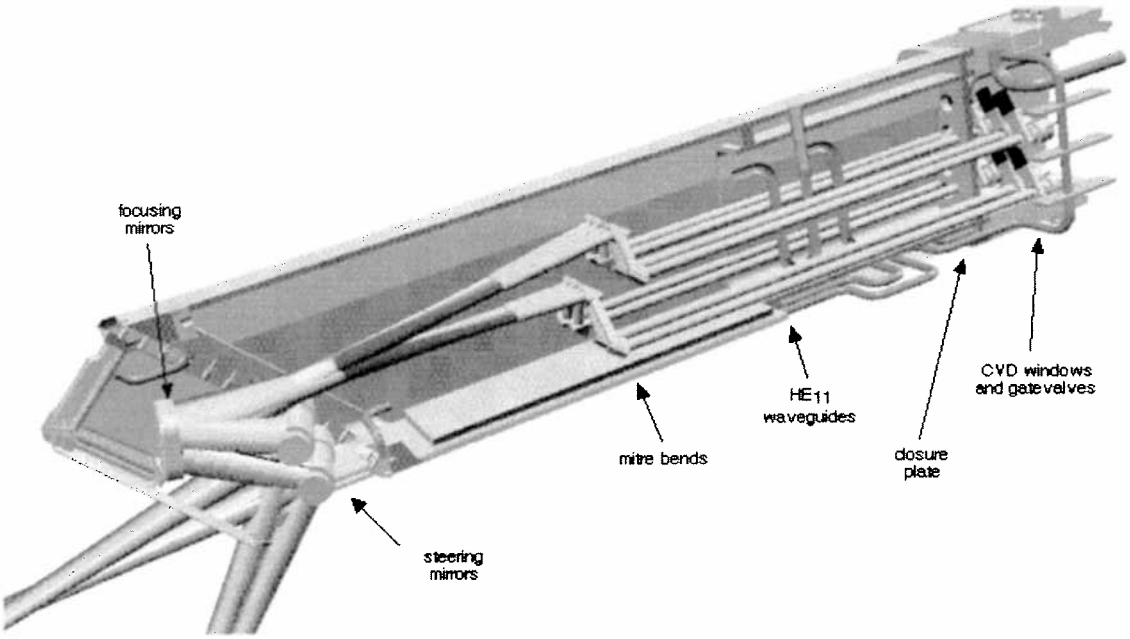

FIGURE 3. The FS launcher installed in the upper port plug.

The ITER transmission line (transmitting the RF power from the gyrotron to the launcher) uses evacuated HE_{11} corrugated waveguide with a nominal inner diameter of 63.5mm [14]. This is a standard size waveguide in use on existing ECH systems [15,16] and is compatible with 2.0MW transmitted power. However, this waveguide size requires a DN100 in-line gatevalve, which has a large actuator severely restricting the available space at the entrance to the port plug. A downtaper to 60mm HE_{11} waveguide (not shown in figure 2 or 3) is inserted just before the launcher, which offers the possibility to use a DN63 in-line gatevalve as planned for the ITER equatorial port FS launcher [17].

The waveguides proceed into the port plug for ~3.0m up to a mitre bend 'dog-leg' assembly. In addition to decreasing the neutron streaming rate in the waveguide, the mitre bend assembly is used to redirect and compress the 8 beams (both in the toroidal and poloidal directions) on to one single focusing mirror, with the incident beams partially overlapping in both directions. The reflected beams are then sent downward to two separate flat steering mirrors, which redirect the beams into the plasma with a toroidal injection angle of β~20°. The free volume in the port plug will be filled with shielding material, which absorbs the neutrons emitted from the burning plasma. The shielding block design (not shown in figure 3) is presented in reference [18].

The steering mechanism [10,19] is the critical component of the FS design and a failure of one steering mechanism would render 4 RF beams unusable. The FS launchers on existing tokamaks have

been crippled when the steering mechanism grips, which typically occurs between two moving surfaces. The steering mechanism proposed for the ITER upper port FS launcher avoids all frictional surfaces. Traditional bearings are replaced with flexure pivots and the movement is controlled using a GHe pneumatic system consisting of bellows pushing against springs, see figure 4. The mirror rotation is controlled by increasing (decreasing) the pressure in the bellows, which will compress (expand) the springs and rotate the mirror downward (upward) for the configuration shown in figure 4. A coiled cooling tube with either a single or double wall is envisioned to provide a flexible coolant feed to the mirror, following a similar design to that proposed for the equatorial launcher [17]. The angular rotation of the steering mirror provides access along the resonance layer from a height of 1.8 to 3.4m (corresponding to a mirror angular rotation of $< \pm 6.3^{\circ}$ or $\pm 12.6^{\circ}$ for the beam), providing access to all relevant q=2 and 3/2 rational flux surfaces as illustrated in figure 1. A more detailed description of the steering mechanism is provided in reference [19].

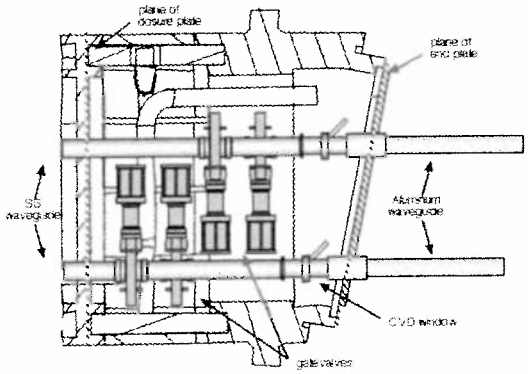

FIGURE 4. Side view of the entrance to the port plug showing the two rows of waveguides along with the gatevalves and CVD diamond window.

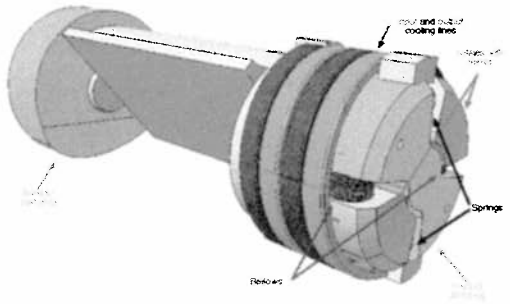

FIGURE 5. Illustration of the proposed frictionless and backlash-free steering mechanism to be used in the FS launcher.

The distance between the waveguide aperture and the focusing mirror is >2.1m, with the beam expanding from ~20mm to 66mm (radius at e^{-1} in E-field) as illustrated in figure 6. The large spot size on the focusing mirror enables to project a very narrow beam waist (19mm) far into the plasma (>1.5m from steering mirror). The beam spot size in free space varies from 19mm to 45mm along the resonance surface. The launcher design is to be optimized to provide the narrowest profile averaged over the range between Z_{min} and Z_{max} (of figure 1). For example, chosing a slightly larger beam waist (~20.5mm) will decrease the average spot size along the resonance surface improving the average NTM stabilization efficiency.

The large spot size on the focusing mirror decreases the power density so that with the 8 overlapping 2.0MW beams, the calculated peak power density is $<1.6 MW/m^2$ (assuming circular polarization and OFHC copper reflective surface at 250°C). The highest peak power density in the launcher occurs on the mitre bend mirrors, where the spot size is relatively small (~20mm). The peak power densities and temperatures occurring on the launcher mirrors are summarized in table 1 (input coolant temperature of 100°C). Note: a surface roughness factor of 1.3 was used for the mitre bend and focusing mirror, while 2.0 was used for the steering mirror (charge exchange neutrals coming from the plasma may degrade the surface quality of the plasma facing mirror). The cooling channels used for calculating the temperature rise were not optimised, with channels dimensions ranging from 5mm by 5mm to 15mm by 5mm at 15 to 30mm intervals and flow rates of 2 to 5m/s. Optimisation of the

cooling channels will be performed in the next design phase. The mitre bend mirror design assumed the coolant could be in direct contact with copper for the miter bend, whereas for the focusing and steering mirror the coolant is in contact with stainless steel to avoid corrosion of copper into the blanket cooling water circuit.

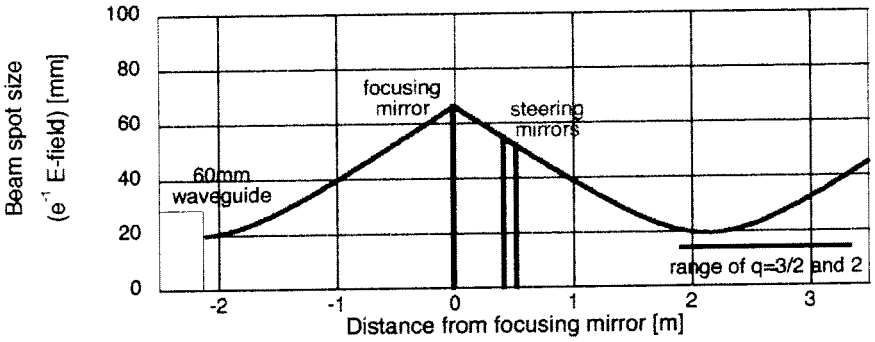

FIGURE 6. The free-space mm-wave beam propagation planned for the FS launcher in the region of the port plug and plasma.

TABLE 1. Power densities and maximum temperatures calculated on the three mirror types in the FS launcher. Absorption coefficient assumes circular polarisation, OFHC copper at 250°C and a surface roughness factor of 1.3 for the mitre bend and focusing mirrors, 2.0 for the steering mirror.

	Mitre bend	Focusing mirror	Steering mirror
Spot size on mirror [mm]	~19	66	~50
Maximum power density [MW/m^2]	<4.7	<1.6	<2.8
Maximum temperature [°C]	228	186	211

3. NTM stabilisation efficiency

Using the beam characteristics of figure 6, the EC driven current profile has been calculated using the beam tracing code ECWGB [11] for the three ITER equilibria (l_i/β_p): EoB2 (0.7/0.65), 3a(0.7,1.0) and 5(1.0,0.8). The narrow beam projected into the plasma by the FS launcher results in a more peaked current density profile achieving $1.55 \leq j_{CD}/j_{BS} \leq 3.47$ for all q=2 and 3/2 surfaces of the calculated equilibria (see figure 7 and table 1) [20]. The FS launcher provides a threefold enhancement over an equivalent 8 port/plug RS launcher and with a total injected power of 20MW was used for these calculations (from 24 1.0MW beams with a transmission efficiency of 83% from gyrotron to plasma).

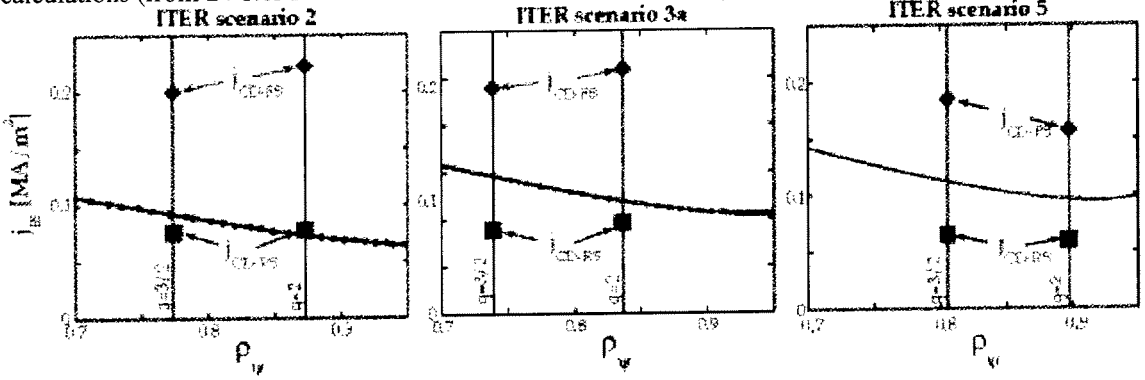

FIGURE 7. The peak driven current density at each the q=2 and 3/2 flux surface compared to the bootstrap current profiles for the three scenarios susceptible to NTMs (2, 3a and 5).

TABLE 2. Comparison of the NTM stabilization efficiency (j_{CD}/j_{BS}) for the relevant rational surfaces and equilibria [5, 20]

	Scenario EoB2		Scenario EoB3a		Scenario EoB5	
	q = 3/2	q = 2	q = 3/2	q = 2	q = 3/2	q = 2
FS Launcher	2.17	3.47	1.55	2.43	1.75	2.15
RS Launcher	0.81	1.07	0.60	0.81	0.59	0.62

4. Extended physics

The ECH system is the only current/heating source on ITER that is both localized and steerable using external actuators. This unique current profile tool offers control of many plasma instabilities beyond NTMs, for example control the sawteeth, FIR and ELMs in addition to current profile tailoring. The front steering launcher design provides the flexibility to expand the role of the upper port launcher, increasing the deposition range beyond the region required for NTM stabilization. The steering mirror is rotated through ±6.3° (equivalent to a beam steering of ±12.6°), to access the region between Z_{min} and Z_{max} (figure 1). However, this range is only a fraction of the steering range feasible of the steering mechanism, ±12° (or ±24° for the beam). The scanning range can be arranged to so that the mirror rotatges further downward to achieve more central deposition and access inside of the q=1 surface as shown in figure 8 for scenario 2, where the beam trajectory has been calculated using the ray-tracing code TORAY-GA [21,22]. Note the steering mirror size would have to be increased (or beam spot size on mirrors decreased) to achieve the steering range of figure 8. Since the flux surfaces are nearly tangential to the resonance surface, there may be a larger current density for central deposition obtained from the upper port FS launcher relative to that offered by the equatorial FS launcher [23], even though the upper port is extremely high and the beam is nearly tangential angle with the resonance.

Accessing inside of the q=1 surface indicates that the launcher may be useful in controlling the sawtooth crash frequency. ECCD deposition inside (outside) the q=1 surface has been shown to shorten (lengthen) the sawtooth period [24]. Shortening the sawtooth period may prevent the onset of the NTM by removing long sawtooth periods, which have been shown to trigger the NTM [25].

The extended range of the FS launcher can also be used to investigate the Frequently Interrupted Regime (FIR) [26] by applying j_{CD} at the edge of the q=4/3 flux surface to modify the shear profile triggering the $4/3^{rds}$ NTM [5]. In such a scenario the degradation associated with the q=2 NTM is diminished by triggering an NTM on the q=4/3 flux surface.

Alternatively, the steering range of the launcher can be increased toward the plasma edge with the potential to trigger the Edge Localized Mode (ELM). The ELM frequency has been increased by driving current locally in the plasma edge [27] which could be obtained by applying j_{CD} at $\rho_{vol} > 0.95$.

Dedicated design and ray tracing calculations are in progress for investigating such potential extended applications of the FS launcher. The upper port launcher may have a higher local current density on some inner flux surfaces than that provided by the equatorial port ECH launcher. Comparison of the current drive efficiency and localization between the two launchers is also under consideration similar to the study performed in reference [23].

5. Conclusions

An FS launcher is being designed for the ITER upper port ECRH launcher and compatible with 2.0MW CW operation. The launcher uses a set of focusing and steering mirrors to decouple the steering and focusing functions of the launcher and achieve a wide steering range and a narrow focused beam along the resonance surface. The steering mechanism (the critical component of the FS launcher) uses a frictionless and backlash-free design in order to have an increased reliability and avoid sticking of the actuator system.

The FS launcher is being designed to optimize the ECH power injected into the ITER plasma, obtaining the maximum performance for each injected megawatt. In the case of NTM stabilisation the mm-wave optics projects a very small beam waist as far as possible into the plasma. The narrow spot size on the resonance results in a high current density relative to the local bootstrap current for the q=2 and 3/2 surfaces of the three scenarios investigated, with NTM stabilization efficiencies in the range of $1.55 \leq \max(j_{CD})/j_{BS} \leq 3.47$. These values exceeds the physics demands for the upper port launcher of $\max(j_{CD})/j_{BS} = 1.2$ and offers a three-fold increase compared to the RS launcher results.

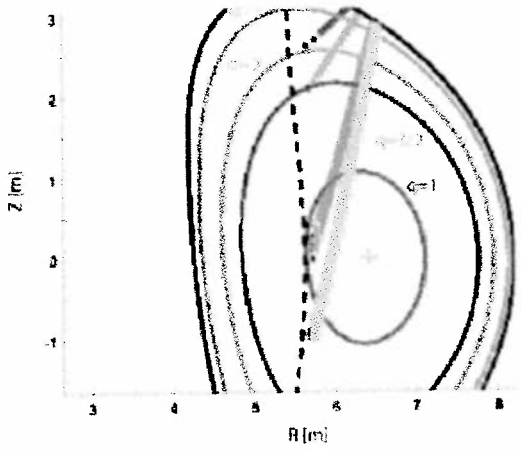

FIGURE 8. The FS launcher can be designed such that access over the range of $0.27 \leq \text{rpsi} \leq 0.95$ from the upper port plug.

The only current source on ITER that is both localized and steerable using external actuators is provided by the ECH launcher systems. This unique current profile tool can also be used to control the sawteeth, FIR and ELMs instabilities, but requires a larger steering range in the plasma. Further design and dedicated beam tracing calculations are to be performed to investigate the practicality of each of these applications.

This work was supported in part by the Swiss National Science Foundation and the European Fusion Development Agreement under the EFDA Technology Programme (contract TW4-TPHE-ECHULB1).

References

[1] Aymer A, Chuyanov V A, Hugnet Y, and Shimomura Y 2001 Nucl. Fusion **41** 1301.

[2] Gantenbein G, Zohm H, Giruzzi G, Günter S, Leuterer F, Maraschek M, Meskat J and Yu Q 2000 Phys. Rev. Lett. **85** 1242.

[3] La Haye R J, Günter S, Humphreys D A, Lohr J, Luce T C, Maraschek M, Petty C C, Prater R, Scoville J T and Strait E J 2002 Phys. Plasmas **9** 2051.

[4] Isayama A, Kamada Y, Ide S, Hamamatsu K, Oikawa T, Suzuki T, Neyatani Y, Ozeki T, Ikeda Y and Kajiwara K 2000 Plasma Phys. Contr. Fusion **42** L37.

[5] Zohm H, Heidinger R, Henderson M, Poli E, Ramponi G, Saibene G, Verhoeven A G A 2005 *Comparison of the performance of different options for the ITER ECRH Upper Launcher* submitted JCPS IAEA-TM on ITER/ECRH.

[6] Sauter O 2004 Phys. Plasmas **11** 4808.

[7] Moeller C P 1998 *A method of remotely steering a microwave beam launched from a highly overmoded corrugated waveguide* Proc. 23rd Int. Conf. on IRMMW.

[8] Verhoeven A G A 2004 *Design of the mm-wave system of the ITER upper port launcher* Proc. 13th ECE & ECH, Nizhny Novograd.

[9] Henderson M A, Chavan R and Sanchez F 2-004 *FS Launcher Study*, Lausanne Research Report, LRP 791/04

[10] Chavan R, Henderson M A and Sanchez F 2005 *An Alternative ECRH Front Steering Launcher for the ITER Upper Port*, accepted for publication in Fusion Engineering and Design.

[11] Farina, D. *et al*, "ECWGB: a beam tracing code for EC heating and current drive", Report FP 03/06 (October 2003), http://www.ifp.cnr.it/

[12] Danilov I, Heidinger R, Meier A and Spaeh P 2005 *Torus window development for the ITER ECRH Upper Launcher* submitted JCPS IAEA-TM on ITER/ECRH.

[13] Henderson M A, Alberti S, Bird J *et al*, 2003 Nucl. Fusion **43** 1487.

[14] ITER detailed Description Document – 5.2 Electron Cayclotron Heating and Current Drive System, G 52 DDD 5 01-05-29 W 0.1.

[15] Goodman T P, Alberti S, Henderson M A, Pochelon A and Tran M Q 1996 Design and installation of the electron cyclotron wave system for the TCV tokamak Proc. 19th Symp. Fus. Tech. Lisbon Portugal ed C Varandas and F Serra (North Holland: Elsevier) pp 565-568.

[16] Lennholm M, Agarici G, Berger-By G *et al*, 2003 Nucl. Fusion **43** 1458.

[17] Takahashi K, Imai T, Kobayashi N, Sakamoto K, Kasugai A, Hayakawa A, Mori S and Mohri K 2005 Fusion Science and Technology **47** 1.

[18] Serikov A, Fischer U, Lang K, Heidinger R, Luo Y and Tsige-Tamirat H 2005 *Radiation shielding analyses for the ECRH launcherin the ITER upper port* submitted JCPS IAEA-TM on ITER/ECRH.

[19] Chavan R, Henderson M A, and Sanchez F 2005 *A Frictionless Steering Mechanism for the Front Steering ECCD ITER Upper Port Launcher* submitted JCPS IAEA-TM on ITER/ECRH.

[20] Ramponi G, Farina D and Nowak S 2005 *Capabilities of the ITER ECRH Upper Launcher at low magnetic fields* submitted JCPS IAEA-TM on ITER/ECRH.

[21] Matsuda K 1989 IEEE Trans. Plasma Sci. **PS-17** 6.

[22] Cohen R H 2002 Phys. Fluids **44**, 139.

[23] Volpe F 2005 *Resiliency of ITER ECRH Upper Launcher to Steering Errors and Changes of Profiles and Integration with Equatorial Launcher* submitted JCPS IAEA-TM on ITER/ECRH.

[24] Angioni C, Goodman T P, Henderson M A and Sauter O 2003 Nucl. Fusion **43** 455.

[25] Westerhof E, Sauter O, Mayoral M L *et al* 2002 Nucl. Fusion **42** 1324.

[26] Gunter S, Maraschek M, de Baar *et al* 2004 Nucl. Fusion **44** 524.

[27] Nave M F, Lomas P J, Huysmans G T A, *et al*, 1999 Nucl. Fusion **39** 1567.

Development of a 2-MW, CW Coaxial Gyrotron at 170 GHz and Test Facility for ITER

J.-P. Hogge[1], S. Alberti[1], A. Arnold[2a,3], D. Bariou[4] , P. Benin[4], T. Bonicelli[5], A. Bruschi[6], R. Chavan[1], S. Cirant[6], O. Dumbrajs[7], D. Fasel[1], F. Gandini[6], E. Giguet[4], T. Goodman[1], R. Heidinger[2b], M. Henderson[1], S. Illy[2a], J. Jin[2a], C. Lievin[4], R. Magne[8], P. Marmillod[1], P.-L. Mondino[5], A. Perez[1], B. Piosczyk[2a], L. Porte[1], T. Rzesnicki[2a], M. Santinelli[9], M. Thumm[2a,3], M.Q. Tran[1,5], I. Yovchev[1]

[1] Centre de Recherche en Physique des Plasmas, Association Euratom–Confédération Suisse, Ecole Polytechnique Fédérale de Lausanne,CH-1015 Lausanne, Switzerland
[2] Forschungszentrum Karlsruhe, Association EURATOM-FZK,
[a] Institut für Höchleistungsimpuls- und Mikrowellentechnik
[b] Institut für Materialforschung, Postfach 3640, D-76021 Karlsruhe, Germany
[3] Universität Karlsruhe, Institut für Höchstfrequenztechnik und Elektronik, Kaiserstr. 12, D-76128 Karlsruhe, Germany
[4] Thalès Electron Devices, 2 Rue de Latécoère, F-78141 Vélizy-Villacoublay, France
[5] European Fusion Development Agreement, Boltzmannstrasse 2, D-85748 Garching bei Muenchen, Germany
[6] Instituto di Fisica del Plasma Consiglio Nazionale delle Ricerche, Via Cozzi 53, I-20125 Milano, Italy
[7] Department of Engineering Physics and Mathematics, Helsinki University of Technology, Association EURATOM TEKES, FIN-02150 Espoo, Finland
[8] Association EURATOM - CEA, Centre d'Etudes de Cadarache, 13108 Saint-Paul-lez-Durance, France
[9] Associazione Euratom-ENEA sulla Fusione, Via E. Fermi 45, P.O. Box 65, I-00044 Frascati (Roma), Italy

E-mail: `jean-philippe.hogge@epfl.ch`

Abstract. In ITER, EC heating and current drive (H&CD) is foreseen not only as a principal auxiliary system for plasma heating and as assist for plasma start-up, but is considered essential in meeting the key requirement of neoclassical tearing mode (NTM) stabilisation, by localized current drive. In the reference ECH design, ITER requires a total of 20MW/CW power at 170GHz using gyrotrons with a unit power of 1MW. A higher power per unit (2MW/gyrotron) would result in a strong reduction of the cost of the whole ECRH system, and would also relax the room constraints on the launcher antenna design. In view of the capability of coaxial cavity gyrotrons demonstrated with short pulse experiments at FZK, the European Fusion Development Agreement (EFDA) has started in 2003 the development of an industrial 170 GHz 2MW/CW coaxial cavity gyrotron, in a collaborative effort between European research associations CRPP/EPFL, FZK, TEKES and Thals Electron Devices (TED). The development plan includes three steps to reach successively 2MW/1s, 2MW/60s and finally 2MW/CW operation. The procurement of the first prototype is in progress and it scheduled to be delivered during the first quarter of 2006. The experimental tests of the prototypes will be carried out at CRPP/EPFL, where an ITER relevant test facility is presently under construction and will be achieved during the second half of 2005. The test facility is designed to be flexible enough, allowing the possible commissioning of tubes with different characteristics, as well the tests of the launcher antenna at full performances.

1. Introduction

In the ITER ECH Reference Design, it is foreseen to inject 20MW/CW of microwave power at 170GHz in the plasma, using gyrotrons with a unit power of 1MW. The main advantages of increasing the unit power of the gyrotrons for the electron cyclotron wave (ECW) system at ITER reside in a more flexible upper port launcher design and in an overall reduction of the installation costs. Coaxial cavity gyrotrons are serious candidates to reach such higher power levels since the inner conductor accumulates the positive effects of mode selectivity and a restriction of beam voltage depression. This matches the choice of a very high order operating mode, and a larger cavity radius in order to maintain the cavity peak ohmic load at a reasonable level ($2kW/cm^2$). Based on short pulse proof of principle experiments carried out at FZK on a 165GHz tube, the European Fusion Development Agreement (EFDA) has launched a collaboration between European institutions and a commercial partner aiming at the development of a 2MW/CW/170GHz coaxial gyrotron. The years 2003 and 2004 were dedicated to a study to demonstrate the technical feasability of a 2MW/CW tube. The development plan foresees to reach the CW regime in three steps: 2MW/1s, 2MW/60s and finally 2MW/CW operation. A contract between the EU and TED was placed by end of May 2004, for the procurement of the first prototype. Even though the target perfomances of this unit are 2MW/1s, it was designed to be fully compatible with CW operation.

In parallel to the gyrotron development, EFDA has placed a contract with CRPP to set up a test stand having the possibility to perform the tests and commissioning of the tube at full performances. It implies deep modifications of the existing infrastructure, the acquisition of new power supplies, the construction of a new dedicated 5-6 MW water cooling system as well as new control and data acquisition systems. The test stand is scheduled to be operative by end of 2005 in a temporary configuration where existing HV power supplies will be used instead of the new ones, the delivery of which will occur later in 2006.

Another contract between EFDA and FZK is running as well. The 165GHz short coaxial tube has been modified to operate at 170GHz, giving the possibility to the community to test the different scientific or technical options envisaged in a high power environment.

In this paper, we concentrate on the gyrotron design, with emphasis on different key aspects of the tube related to the high power and long pulse operation. The future test stand is then briefly described.

2. Gyrotron design

The design of the 170GHz/CW tube was largely based on the experimental results obtained on a 165GHz short pulse tube operated at FZK, which gave a proof of principle of the coaxial gyrotron ability to generate radiation in excess of 1MW at frequencies relevant to ITER. The dimensions of the existing tube as well as the magnetic field topology were used as a starting point for the design of the CW version.

The experience acquired during the development of the 0.5MW/118GHz/600s tube for CRPP and CEA, the 1MW/140GHz/CW for W7-X, was applied to the technical design in terms of options adopted for the cooling of different subassemblies, stray radiation handling and optimization of the RF output profile.

The main characteristics of the first prototype tube are summarized in table 1, and a sketch of the tube is given in figure 1.

A particular feature of the tube is that the RF structure (cavity, launcher, mirror system, mirror box) is at the depressed potential (+35 kV). Therefore, the use of an insulator between the tube and the superconducting magnet (SCM) , as well as an insulating ceramic ring between the mirror box and the collector is necessary. A DC-Break will be placed between the gyrotron window and the next item (either the RF Conditioning Unit (RFCU) or an RF load).

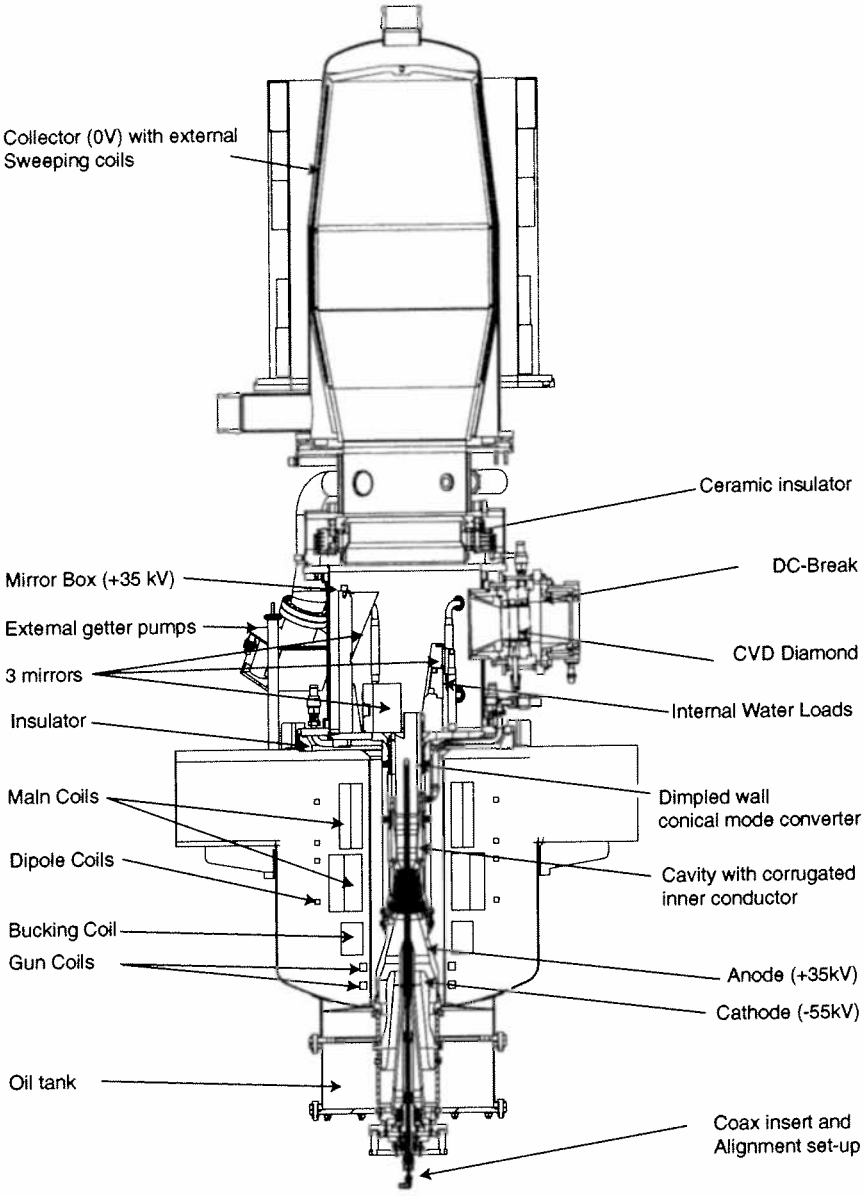

Figure 1. Sketch of the 2MW/CW 170GHz gyrotron.

2.1. Electron Gun

The coaxial magnetron injection gun (CMIG) assembly is shown in Fig. 2, together with the coaxial insert. At the nominal beam current, the emitting current density is of the order of 4.2A/cm^2. The electrodes have been shaped to limit the peak electric field at values $< 7\text{kV/mm}$. Preventing the possible built up of a Penning discharge, i.e. the trapping of electrons in regions with a defavorable magnetic field lines – equipotentials topology [1], was achieved by tapering the rear part of the cathode and the coaxial insert, with the additional beneficial effect of increased mechanical stability.

The electron beam characteristics at the nominal parameters were estimated using DAPHNE

Table 1. Main characteristics of the 2MW/170GHz/CW tube.

Parameter	Value	Parameter	Value
Frequency	170 GHz	Cavity peak losses	1.7kW/cm^2
Magnetic field	6.86 T	Cavity total losses	45kW
Operating mode	$TE_{34,19}$	Insert peak losses	.2kW/cm^2
Cathode voltage	-55 kV	Insert total losses	2kW
Body voltage	+35 kV	Stray radiation losses	100kW
Beam current	75 A	Window	CVD diamond
RF output power	2 MW	Window diameter	96 mm
Power modulation	0.6 - 2MW	Window losses	880W
Efficiency	45%	Collector loading (CW)	2.4MW
Beam radius	10 mm	Collector loading (modulated operation)	3.1 MW
Velocity ratio	1.3	Single-stage depressed collector	–
Modulation frequency	5kHz		

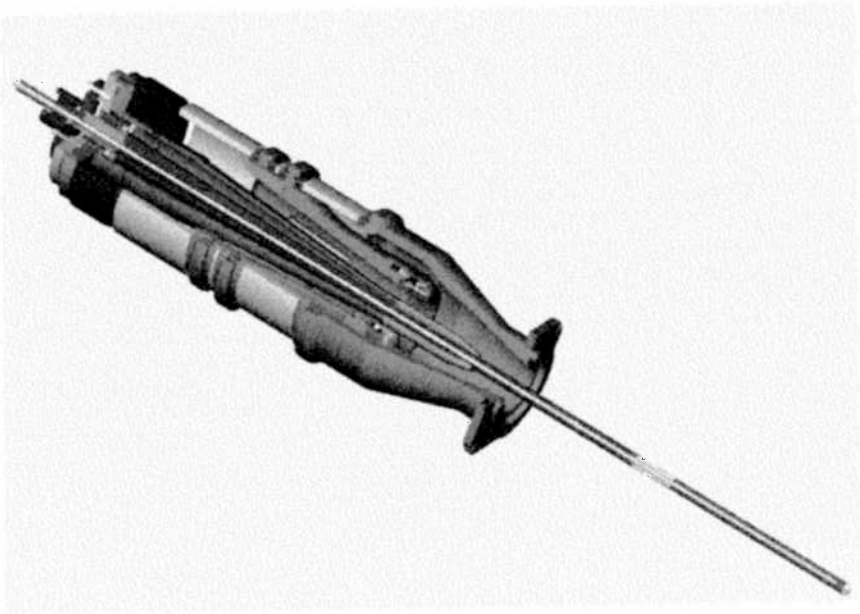

Figure 2. The electron gun and coaxial insert assembly.

[4] are summarized in table 2. The type of electron flow is intermediate, i.e. neither laminar nor non-laminar [5].

A parametric study of the electron beam parameters sensitivity on a possible placement inaccuracy of the superconducting magnet coils was performed in order to validate the magnetic field topology. Even though their nominal value is null, a proper choice of the gun coil currents (see fig. 1) can compensate for a ± 0.5mm longitudinal shift of the bucking coil without any loss of quality. This is well with the mechanical tolerances.

Table 2. Electron beam characteristics obtained with DAPHNE at the nominal parameters $I_b = 75$A, $U_{cath} = -55$kV, $U_{body} = +35$kV, $B_{cav} = 6.86$T.

Parameter	Value	Spread (rms value, %)
Beam radius R_b, mm	10.00	1.29
Transverse velocity, $\beta_\perp$	0.413	0.72
Axial velocity, $\beta_\parallel$	0.317	1.21
Velocity ratio $\alpha = \beta_\perp/\beta_\parallel$	1.30	1.92
Relativistic factor γ	1.171	-
Beam depression , kV	2.6	-
Magnetic compression ratio	34.5	-
Current density at emitter, A/cm^2	4.41	-
Electric field at the emitter, kV/mm	4.6	
$E \cdot V$ at the emitter, kV^2/mm	416	

2.2. Coaxial Insert

This component is 1.2m long and shall be adjusted during operation with an accuracy of a few tenths of a millimeter with respect to the cavity wall using a 2D microactuator. The inner conductor alignment will be performed at reduced parameters by using a set of dipole coils in the gyrotron magnet. The required accuracy in the concentricity of the inner conductor to the cavity is 0.05mm. A mock-up coaxial insert made of Glidcop and stainless steel was realised to validate the assembling process. The design of the cooling circuit was improved to avoid turbulences giving rise to vibrations incompatible with a reliable and stable operation of the gyrotron. It will be performed by means of a coaxial water flow.

In addition, the structure was vibrated according to a road transport gauge. Potentially harmful resonances at frequencies of 22 Hz, 80 Hz and 160Hz were identified. Since the structure is relatively fragile, the coaxial insert support will be improved to give the possibility to lock its postion during transportation.

2.3. Cavity

The cavity profile was designed in order to optimize the RF output, with the constraint of keeping the peak wall ohmic loading at an acceptable value of 1kW/cm^2 (ideal copper at room temperature). The outer part consists in a linear input taper, a cylindrical section in which the interaction takes place, a linear output taper and finally a non-linear output taper which ensures that the power mode conversion of the $TE_{34,19}$ to modes with a different radial index is $< 0.2\%$. The beneficial effects of the coaxial insert are the minimization of the beam depression by fixing a potential close to the electron beam, and mode selectivity. The latter feature is even enhanced if the insert is tapered and if longitudinal corrugations are cut in it [2]. In the present case, the insert downtaper angle is 1 deg and it has 75 corrugations with a depth of the order of 0.44 mm. Multimode time-dependent simulations have shown that the nominal mode $TE_{34,19}$ is dominant over a wide range of parameters. The effect of cavity thermal deformations was taken into account in an iterative procedure with the result that the position of the maximum of the electric field is shifted by 2 mm with no other major change.

Taking into account the Glidcop resistivity and a surface roughness factor of 1.5 (estimation based on thermal measurements on the 140 GHz gyrotron), it is estimated that the actual peak wall ohmic loading will be of the order of $\rho_{\text{cavity}} = 1.7$kW/cm^2 (compared to 1kW/cm^2 in the ideal case), corresponding to a total ohmic power dissipated in the cavity of 45 kW.

With the same arguments, the ohmic loading on the insert is expected to be of the order $\rho_{\text{insert}} \simeq 0.1\text{kW/cm}^2$ in the cavity, and the total losses on the insert $\simeq 0.4\text{kW}$.

The cooling of the cavity will be performed by a diphasic cooling structure ('Rachig Rings'). A mock-up test has successfully shown the effectiveness of the cooling system, with a measured heat exchange coefficients as high as $0.15\text{W}/(\text{mm}^2 \cdot \text{K})$.

2.4. Dimple Wall Launcher and Quasi-Optical Mirror System

The mode $TE_{34,19}$ is not ideal for conversion to a Gaussian beam and the edge diffraction losses of the conical dimple wall mode converter and quasi-optical mirror system were initially estimated to 10% of the RF output power. The key parameter in the optimization procedure of the launcher wall perturbations and the mirrors system was the minimization of edge diffraction losses at the cuts, around the mirrors and at the window [6]. The dimples combine $\Delta m = 1, 2, 3$ corrugations. The wall currents as a function of the longitudinal position and the azimuthal angle are shown in fig. 3, in 3dB steps down to -30dB. The red path corrresponds to the location of the cut.

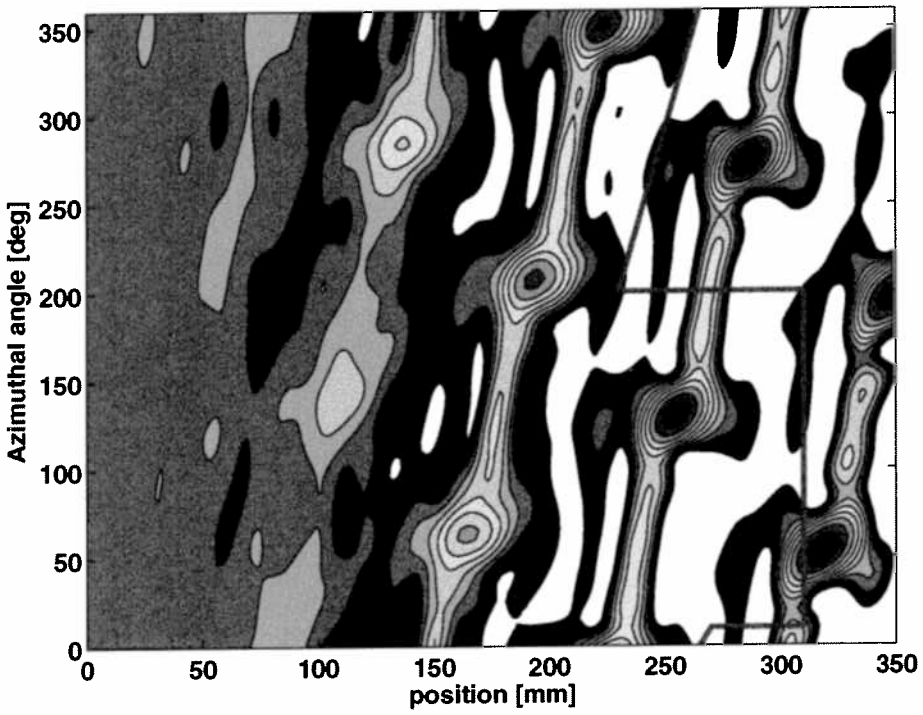

Figure 3. Wall currents in the launcher, in 3dB steps. The red path indicates the launcher cut.

The quasi-optical mirror system consists in three mirrors: (1) A quasi-elliptical mirror collects as much power radiated from the launcher as the room constraints allow and reflects a non divergent wave beam. (2) The second mirror has a quadratic (toroidal) shape. (3) The last mirror has a non-quadratic surface contour optimized to maximize the Gaussian beam content at the window and to minimize window edge losses. The cost of minimization is a decrease of the beam quality.

2.4.1. Initial Quasi-Optical Mirror System Two complete systems consisting of a dimple wall mode converter and a mirror system were built and tested at low power level ($\simeq$ 1 mW) and at

high power on the modified FZK coaxial tube. Both results were coherent with each other, but exhibited a significant difference with numerical predictions. The discrepancy was attributed to the fact that the $\Delta m = 2$ launcher corrugations were mistreated when designing the mirror system. A proper handling of the launcher profile would allow the simulation to reproduce the cold and hot profiles [7].

2.4.2. Modified Quasi-Optical Mirrors System Correctly taking into account the $\Delta m = 2$ launcher corrugations, the shapes of the second and third mirrors were modified and will be cold tested soon. The computed power distributions at the window plane and 1m outside the window plane are shown in figs. 4 and 5 in 3dB steps.

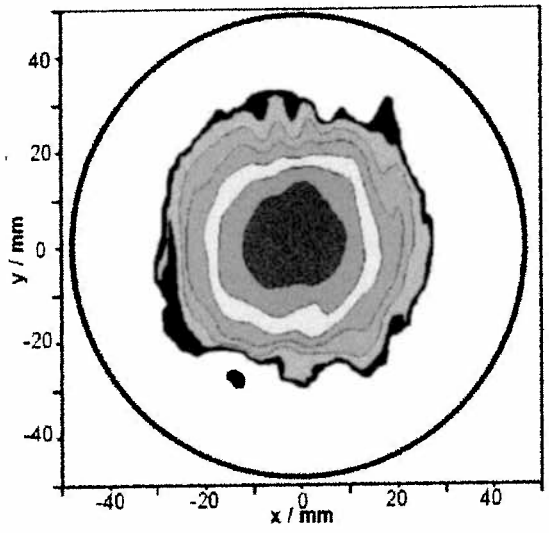

Figure 4. Power distribution in the window plane, for the improved mirror system, shown in 3dB steps.

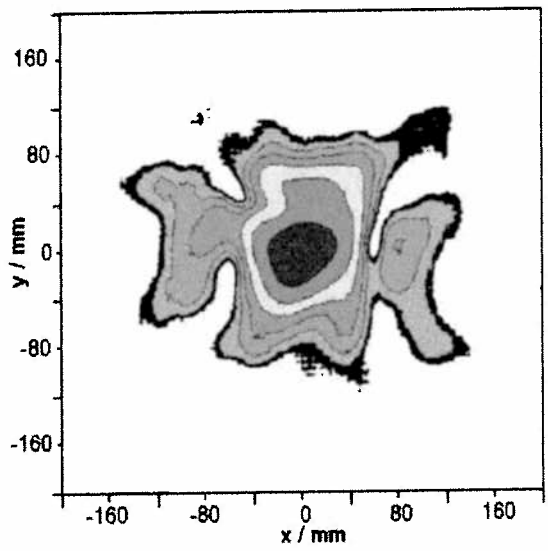

Figure 5. Power distribution 1m after the window plane, for the improved mirror system, shown in 3dB steps.

2.5. Internal Loads and Stray Radiation Handling

A particular care was brought to the handling of stray radiation inside the tube which is identified as the main issue toward the achievement of CW operation .

Internal water loads consisting in a water cooled ceramic tube will be placed inside the tube to evacuate efficiently trapped radiations. The advantage of internal loads with respect to a conventional relief window resides in the number of loads which can be accommodated in the tube, leading to a higher equivalent surface to evacuate stray radiation. Shown on fig. 6 is a pair of internal loads, and in fig. 7 the arrangment of 6 such loads in the tube.

The amount of stray microwave losses inside the gyrotron tube has been determined to be as high as about 8 % of the microwave output power. A test of internal microwave absorbers consisting of four water cooled Al_2O_3 tubes has been performed and placed inside the mirror box. It has been measured that the internal microwave load is absorbing a power of $0.022 * P_{out}$ corresponding to more than 25% of the stray losses. High power tests are scheduled in the first trimester 2005 with the 140GHz/1MW gyroton. The thermal limit of the component would be checked by placing the ceramic close to propagation axis of the RF beam. The vacuum reliability is also under investigation, with cyclic thermal heat treatments.

Figure 6. Internal loads.

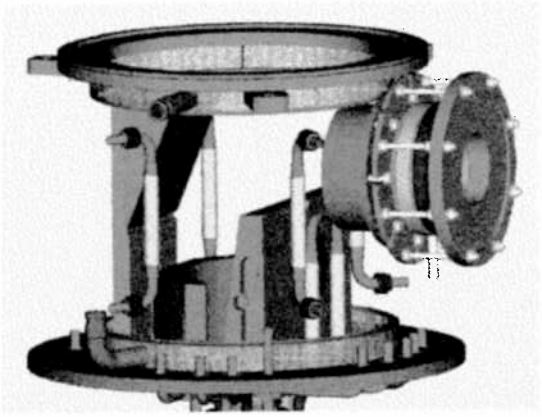

Figure 7. The mirror box.

The mirror box itself has a double-wall structure and computations have shown that it can evacuate 100kW safely.

2.6. Window

The output vacuum window is made of a water edge-cooled CVD-diamond disk brazed to 96 mm clear aperture copper cuffs. A specific high temperature brazing process increases the reliability and simplifies the operating conditions without requiring anti-corrosion additives.

2.7. Collector

The collector is a critical component of the tube. During operation at full parameters, the loading will be of the order of 2.2 MW. During the first phase of the design, it was foreseen to have a coaxial design with the sweeping coils located in the central part. More accurate simulations conducted during the second phase have shown that this geometry would marginally allow the evacuation of the deposited energy, and have led us to abandon this option.

With respect to the first design phase [8], the collector diameter was increased to 600mm and the 6 sweeping coils are now external. The simulations have been refined to account for the eddy currents flowing in the wall, which have a shielding effect and prevent the magnetic field to penetrate into the collector [9]. The electron trajectories used to estimate the collector power deposition are taken from a self-consistent monomode simulation.

The simulations results indicate that it is possible to find a sweeping coils currents combination leading to a maximal peak power density < 500 W/cm^2, showing that this is a usable collector design. Additional optimizations are nevertheless needed to make the peak power density less sensitive to a variation of the external parameters.

2.8. RF Conditioning Unit

The design of the RFCU was dictated by the need of flexibility. It consists in 5 mirrors located on an horizontal plane (see fig. 8. The first one (1) is planar and will be used to compensate for any misalignment of the gyrotron output beam. Two quadratic mirrors (2 and 5) will be used to match the beam to the HE11 mode of the transmission line while minimizing the peak power density on the universal polarizer made of two gratings (3 and 4). The alignment of such an in-plane arrangment is easy: mirrors 1,2 and 5 must be rotated around 2 axes, whereas the polarizer have only to be rotated around an axis normal to their surface.

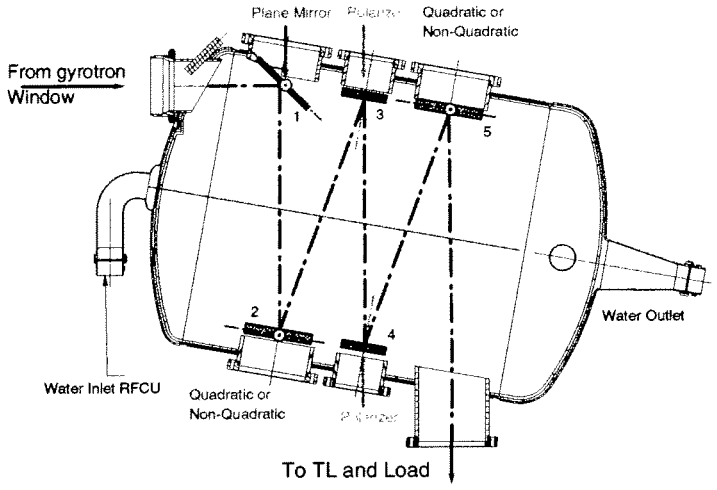

Figure 8. RF conditioning unit (RFCU).

In case the output beam profile at the window would lead to unacceptable edge diffraction losses and/or to a poor coupling to the HE_{11} mode, it is envisaged to to use a quadratic first mirror and synthetized mirrors 2 and 5. The RFCU cooling has been dimensioned to evacuate as much as 80kW.

3. Test Stand

It is foreseen to test the gyrotron tubes at the CRPP. A test stand, able to provide the electrical power, and with a 5-6 MW /CW cooling capability is being built and will be available for the beginning of the tests.

3.1. Electrical Power Supplies

A design study of the power supplies has been performed by different Associations as an ITER task. The electrical supply scheme is depicted in fig. 9

3.1.1. Long Term Power Supplies The Main High Voltage Power Supply (MHVPS) fixes the cathode potential with respect to ground (55kV nominal, 60kV max.) and delivers the electron beam current (75A). Its shutdown time is $30\mu s$. A PSM like (pulse step modulator) option has been retained.

The Body Power Supply (BPS, 40kV, 150mA static, <5A transient) is connected between the body and the grounded collector. It is responsible for the cathode to body potential regulation with an accuracy of $\pm 0.5\%$, and provides the modulation capability (25kV peak-to-peak) at frequencies up to 5kHz. The minimal modulation frequency is fixed by the maximal thermal loading that the collector can stand. The construction of the BPS will be PSM based as well. In order to limit the fault energy in the gyrotron to a value <10J in case of failure or arc, a High Voltage Solid State Switch (HVSSS), equipped with IGBT's (Isolated Gated Barrier Transistor) will be used. Beyond the protective usage of this device, it can also be used to make on-off modulation of the electron beam (with the advantage that there is no collector loading during the off phase) at frequencies up to 5kHz.

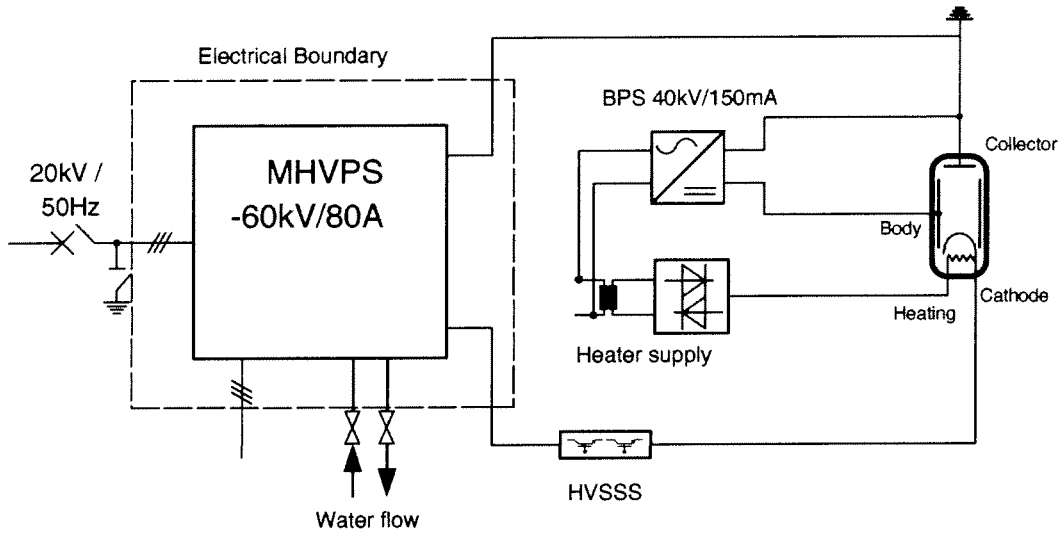

Figure 9. Electrical supply scheme.

3.1.2. Temporary Power Supplies (Plan B) The delivery of the above mentioned power supplies is scheduled approximately 9 months after that of the gyrotron and the SCM. During the first stage of experiments, an existing 85kV/80A power supply operated on the TCV ECRH system (RHVPS) will be used to perform the initial short pulse tests. Because of the relatively far location of the RHVPS ($\simeq$ 100m from the tube), a crowbar is foreseen (see fig. 10). If desired, it might also be possible to use a BPS to reach the nominal accelerating voltage.

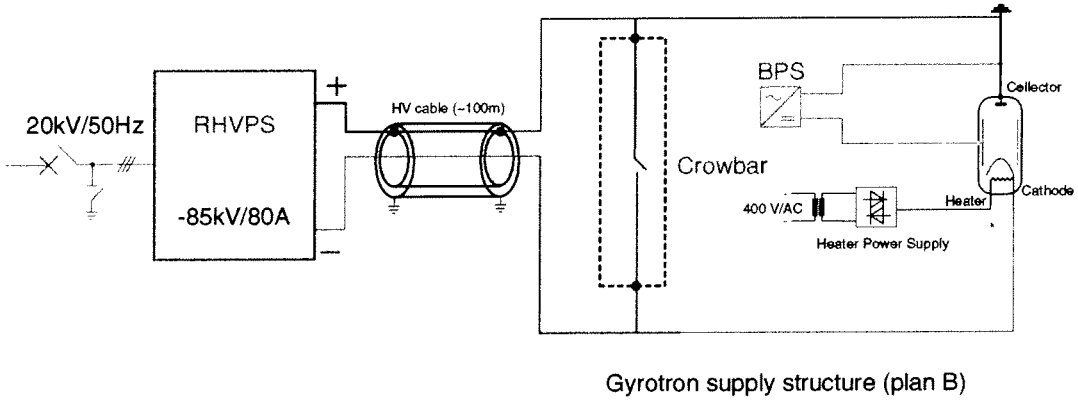

Figure 10. Temporary Electrical supply scheme (plan B)

3.2. Cooling Set-Up

The cooling system has been designed to be compliant with the ITER DGR1 (Design Requirements and Guidelines Level 1): Nominal inlet temperature: $T_{in} = 40°$, maximum outlet temperature: $T_{out} = 70°$, nominal inlet pressure: $P_{in} = 6$bars. It will consist in three separate circuits dedicated to the collector, the auxiliaries and the RF load.

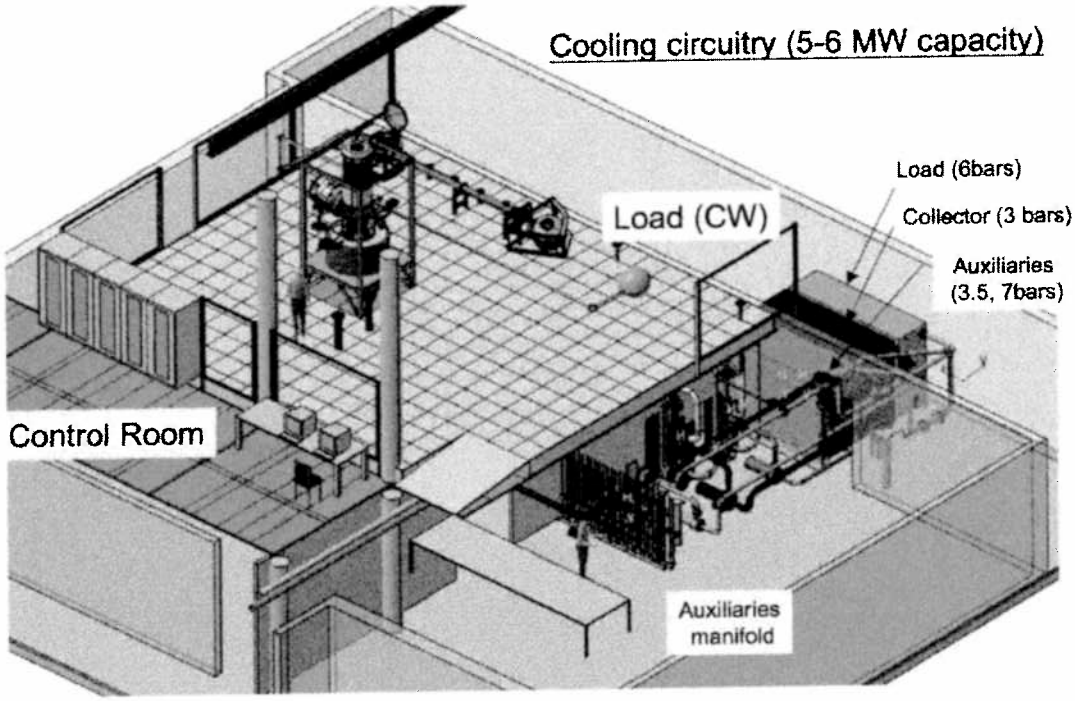

Figure 11. Sketch of the 2MW/CW test stand.

A view of the Test stand as it will appear is shown on fig. 11. The Test stand is scheduled to be ready for operation by end of 2005.

4. Present status and conclusion

A contract has been placed by the European Commission with TED for the production of the first one of three 2MW/170GHz gyrotron prototype. The target performance of the tube is 2MW/1s, but the design is CW compatible. The delivery is scheduled for the end of the first quarter 2006, approximately at the same time as the Superconducting Magnet. Due to the later delivery of the power supplies, existing ones will be temporarily used. The test stand infrastructure is being set-up and should be operative for end of 2005.

Acknowledgments

The work at CRPP is partially supported by the Swiss National Science Foundation.

References

[1] B. Piosczyk, G. Dammertz, O. Dumbrajs, M. Kartikeyan, M. Thumm and X. Yang, 165-GHz Coaxial Cavity Gyrotron, IEEE Trans. Plasma Science **32**(3), 853 (2004).
[2] O. Dumbrajs, A Novel Method of Improving Performance of Coaxial Gyrotron Resonators, IEEE Trans. Plasma Science **30**(3), 836 (2002).
[3] O. Dumbrajs and G. Zaginaylov Ohmic Losses in Coaxial Gyrotron Cavities With Corrugated Insert, IEEE Trans. Plasma Science **32**(3), 861 (2004).
[4] T.M. Tran, R. Gruber and S. Merazzi, DAPHNE, a 2D Axsisymmetric Electron Gun Simulation Code, Proc. of the 6th Joint EPS-APS Int. Conf. on Physics Computing,EPS, Petit-Lancy, 492 (1994).
[5] I. Yovchev, J.-P. Hogge, T.P. Goodman, S. Alberti and T.M. Tran, Design of the ITER 170 GHz Gyrotron

Gun, Proc. of the Joint 29th Int. Conf. on IR&MM Waves and 12th Int. Conf. on THz Electronics, Karlsruhe, Germany, 645 (2004).

[6] J. Jin, B. Piosczyk, G. Michel, M. Thumm, O. Drumm, T. Rzesnicki and S.C. Zhang, The Design of a Quasi-Optical Mode Converter for a Coaxial Cavity Gyrotron, Proc. of the Joint 29th Int. Conf. on IR&MM Waves and 12th Int. Conf. on THz Electronics, Karlsruhe, Germany, 669 (2004).

[7] B. Piosczyk, T. Rzesnicki, G. Dammertz, O. Dumbrajs, S. Illy, J. Jin, W. Leonhardt, G. Michel, M. Schmid, M. Thumm, O. Drumm, and X. Yang, A 2MW, 170 GHz Coaxial Cavity Gyrotron – experimental verification of the design of main components, This conference.

[8] J.-P. Hogge, S. Alberti, A. Arnold, D. Bariou, P. Benin, A. Beunas, T. Bonicelli, R. Chavan, S. Cirant, O. Dumbrajs, O. Drumm, D. Fasel, E. Giguet, T. Goodman, M. Henderson, S. Illy, J. Jin, G. LeCloarec, C. Lievin, R. Magne, P.-L. Mondino, B. Piosczyk, L. Porte, T. Rzesnicki, M. Santinelli, A.B. Sterck, M. Thumm, M.Q. Tran, A.G.A. Verhoeven and I. Yovchev, Development of a 2MW, CW, 170GHz Coaxial Cavity Gyrotron for ITER, Proc. of the 13th Joint Workshop on Electron Cyclotron Emission and Electron Cyclotron Heating, 17–20 May 2004, Nizhny Novgorod, Russia, 393 (2005).

[9] S. Illy, B. Piosczyk, I. Danilov and S. Raff, Design Studies of the Collector Sweeping System for the 2MW 170 GHz Coaxial Gyrotron for ITER, Proc. of the Joint 29th Int. Conf. on IR&MM Waves and 12th Int. Conf. on THz Electronics, Karlsruhe, Germany, 231 (2004).